Remote Sensing of Environment 280 (2022) 113223

Contents lists available at ScienceDirect

Remote Sensing of Environment

journal homepage: www.elsevier.com/locate/rse

Generating 5 km resolution 1981–2018 daily global land surface longwave radiation products from AVHRR shortwave and longwave observations using densely connected convolutional neural networks

Jianglei Xu [a,*], Shunlin Liang [b,c,*], Han Ma [c], Tao He [a]

[a] School of Remote Sensing and Information Engineering, Wuhan University, Wuhan 430079, China
[b] Department of Geographical Sciences, University of Maryland, College Park, MD 20742, USA
[c] Department of Geography, University of Hong Kong, Hong Kong 999077, China

ARTICLE INFO

Edited by Jing M. Chen

Keywords:
Surface longwave radiation
AVHRR
Deep neural network
Long time series
Shortwave observation

ABSTRACT

Surface longwave radiation (SLWR) components, including downward longwave radiation (DLR), upward longwave radiation (ULR), and net longwave radiation (NLR), are major contributors to the Earth's surface radiation budget and play important roles in ecological, hydrological, and atmospheric processes. Previous SLWR products have different drawbacks, such as being temporally short (after 2000), spatially coarse ($\geq$ 25 km), and instantaneous values, which hinder their in-depth applications in land surface process modeling and climate trends analysis. Here, we reported the Advanced Very High-Resolution Radiometer (AVHRR)-based Global LAnd Surface Satellites (GLASS-AVHRR) SLWR products over the global land surface at a 5 km spatial resolution and 1 day temporal resolution between 1981 and 2018. These products were generated using multiple densely connected convolutional neural networks (DesCNNs) from the AVHRR top-of-atmosphere (TOA) reflected and emitted observations and European Centre for Medium-Range Weather Forecasts (ECMWF) fifth generation reanalysis (ERA5) near-surface meteorological data. DesCNNs were trained using integrated SLWR samples derived from the Moderate Resolution Imaging Spectroradiometer (MODIS)-based GLASS, Clouds and the Earth's Radiant Energy System Synoptic (CERES-SYN), and ERA5 SLWR products. In situ measurements from 231 globally distributed sites were used to evaluate the GLASS-AVHRR SLWR estimates. The results illustrated the overall high accuracies of GLASS-AVHRR SLWR products with root-mean-square-errors (RMSEs) of 18.66, 14.92, and 16.29 Wm^{-2}, and mean bias errors (MBEs) of −2.69, −3.77, and 0.49 Wm^{-2} for all-sky DLR, ULR, and NLR, respectively. We found good correlation and consistency between GLASS-AVHRR and both CERES-SYN and ERA5 in terms of spatial patterns, latitudinal gradient, and temporal evolution. Our results revealed the significant contribution of shortwave observations to SLWR estimation owing to the high amounts of clouds over polar regions and water vapor and clouds in tropical areas, which was not previously widely recognized by the remote sensing community. GLASS-AVHRR SLWR products were updated, documented, and made available to the public at www.glass.umd.edu and www.geodata.cn.

1. Introduction

Surface longwave radiation (SLWR) in the thermal-infrared range (4–100 μm) is an important component of the surface radiation budget at the surface-atmosphere interface and determines the thermal conditions of the land, oceans, and atmosphere (Trigo et al., 2010; Liang et al., 2019; Liang et al., 2010). SLWR is valuable for both scientific and industrial applications related to agriculture, land surface modeling, and climate monitoring. Three specific longwave radiation components constitute SLWR, i.e., downward longwave radiation (DLR)—emitted from the atmosphere to the surface—upward longwave radiation (ULR)—representing the capability of the thermal radiation from the Earth's surface—and net longwave radiation (NLR), which is the difference between DLR and ULR. As important input parameters for land surface processing models, accurate SLWR estimates are urgently needed in the meteorological, hydrological, and agricultural communities (Wang et al., 2017; Wang and Liang, 2009a; Zhou et al., 2007; Ruckstuhl et al., 2007). For instance, SLWR estimates of <20 and 10 Wm^{-2} at

* Corresponding authors.
E-mail addresses: jiangleixu@whu.edu.cn (J. Xu), sliang@umd.edu (S. Liang).

https://doi.org/10.1016/j.rse.2022.113223
Received 11 March 2022; Received in revised form 19 July 2022; Accepted 13 August 2022
Available online 23 August 2022

instantaneous and monthly time scales, respectively, are acceptable uncertainty levels for meteorological applications (Ellingson, 1995; Gupta et al., 2004; Schmetz, 1989a); however, most currently available SLWR products cannot meet this need (Gui et al., 2010; Zeng et al., 2020; Tang et al., 2021). Moreover, as effective diagnostic parameters for climate change, a long-term, high-resolution, and spatially continuous SLWR dataset is indispensable for accurate characterization and quantification of spatiotemporal variation in the surface radiation budget at the global scale (Wei et al., 2021; Frederick and Tinsley, 2018; Yeo et al., 2018; Dewitte and Clerbaux, 2018; Koll and Cronin, 2018; Kofroňová et al., 2019).

Spatiotemporally continuous SLWR estimates are generally available from numerical modeling (e.g., atmospheric reanalysis) and satellite-derived products. The most attractive advantages of numerical modeling are spatially continuous distribution and long period, which facilitate climate trends analysis (Jia et al., 2020; Gao et al., 2020; Liu et al., 2021). However, the large uncertainty and spread and coarse spatial resolution ($> 0.5^{\circ}$) hinder their in-depth application in spatiotemporal variations at a regional scale (Wang and Dickinson, 2013; Wild et al., 2001; Lindsay et al., 2014; Newman et al., 2000).

Satellite observations offer an affordable alternative for estimating SLWR with sufficient spatial and temporal sampling resolutions. Similar to numerical modeling, satellite-derived SLWR estimates retain good spatiotemporal continuity but with generally lower uncertainty and finer spatial resolution (Gui et al., 2010; Tang et al., 2021; Zeng et al., 2020). Many regional- and global-scale algorithms have been developed from polar-orbiting satellites (e.g., Moderate Resolution Imaging Spectroradiometer, MODIS (Wang and Liang, 2009; Wang et al., 2009; Cheng et al., 2017)), and geostationary satellites (e.g., the Geostationary Operational Environmental Satellites, GOES (Wang and Liang, 2010; Qin et al., 2021; Zhu et al., 2021)). Satellite-derived SLWR products include the Clouds and the Earth's Radiant Energy System Synoptic $1^{\circ} \times 1^{\circ}$ (CERES-SYN (Rutan et al., 2015b)), Global Energy and Water Cycle Experiment-Surface Radiation Budget (GEWEX-SRB (Gupta et al., 2008; Stackhouse Jr et al., 2000)), and International Satellite Cloud Climatology Project-Flux Data (ISCCP-FD (Zhang et al., 2004)). Additionally, the Global LAnd Surface Satellite products suite (Liang et al., 2021b) provides MODIS-based instantaneous SLWR values at 1 km spatial resolution (GLASS-MODIS (Cheng et al., 2017; Cheng and Liang, 2016)).

Multiple studies have been conducted to evaluate SLWR estimates from these satellite-derived products and atmospheric reanalysis (Zeng et al., 2020; Tang et al., 2021; Gui et al., 2010; Wang et al., 2021b). Gui et al. (2010) evaluated three SLWR products and found that the CERES SLWR components had higher accuracy than the GEWEX-SRB and ISCCP-FD products, with standard derivation of differences of 21.8 and 21.9 Wm^{-2} for DLR and ULR, respectively. Tang et al. (2021) showed that the European Centre for Medium-Range Weather Forecasts (ECMWF) fifth generation reanalysis (ERA5) DLR retrievals had a root-mean-square-error (RMSE) of 21.9 Wm^{-2} over land, which was better than that of CERES-SYN (RMSE of 26.0 Wm^{-2}); however, ERA5 DLR retrievals performed slightly worse than CERES-SYN over oceans. Additionally, Wang et al. (2021b) compared seven SLWR datasets at the three poles, including two satellite-based products (CERES-SYN, APP-x) and five atmospheric reanalysis products (ERA5, MERRA-2, CFSR, JRA-55, and GLADS). The evaluation results demonstrated that ERA5 and CERES-SYN DLR had better accuracies, both yielding mean bias errors (MBEs) and RMSEs of <7 and 25 Wm^{-2}, respectively. Generally, CERES-SYN and ERA5 provide better SLWR estimates at a global scale than other atmospheric reanalysis and satellite-derived products. However, the short period (after 2000) and coarse spatial resolution (1°) limit the application of CERES-SYN in climate trends analysis. Additionally, the coarse spatial resolution (0.25°) of ERA5 implies insufficient spatial variation of the SLWR at a regional scale when applied in meteorological, hydrological, and agricultural research. Therefore, a long-term, spatiotemporally continuous, high-resolution SLWR dataset is still needed for the current global climate trends analysis and regional hydrological and agricultural applications.

The Advanced Very High-Resolution Radiometer (AVHRR) sensor has collected space observations at ~1.1 km nadir spatial resolution almost continuously since 1981 based on multiple National Oceanic and Atmospheric Administration satellite platforms; the data provide an opportunity to explicitly replicate the long-term spatiotemporal variation of global SLWR (Chen et al., 2018; Casey et al., 2010). Much effort has been made to retrieve long-term SLWR records from AVHRR data in the past decade. The CMSAF Cloud, Albedo, and Surface Radiation dataset from AVHRR data (CLARA-A2) have provided monthly DLR on a 0.25° grid system for 34 years (Karlsson et al., 2013; Karlsson et al., 2017). However, large uncertainty in the CLARA-A2 DLR retrievals arises owing to the cloud fraction to a simple weighted average of clear-sky ERA-Interim values (Urraca et al., 2017). Moreover, no data are available over snow-covered surfaces owing to reduced data quality. The long-term spatiotemporal distribution of surface SLWR is alternatively available from the Cloud_cci AVHRR post meridiem (AVHRR-PM) dataset (Stengel et al., 2020), which was generated using the atmospheric radiative transfer (Fu and Liou, 1992). The AHVRR-PM dataset provides instantaneous SLWR retrievals at a 0.05° spatial resolution; however, the product cannot solve the diurnal variation of SLWR, which is one of the implementation requirements documented by the Global Observing System for Climate (GCOS; https://gcos.wmo.int/en/gcos-implementation-plan). Consequently, we aimed to generate a long-term (1981–present), high-resolution (5 km), spatiotemporally continuous daily mean SLWR dataset from AVHRR observations to support climate modeling and meteorological applications.

Algorithms for estimating SLWR from satellite observations have been continuously developed in the past three decades and can be roughly categorized into three groups, i.e., physical, parameterized, and hybrid methods (Jiao and Mu, 2022). Physical methods use a radiative-transfer model (RTM) driven by satellite-derived atmospheric profiles to calculate SLWR (Viúdez-Mora et al., 2009). However, inefficient computation of RTM and unavailability of specific atmospheric profiles result in the unrealistic application of physical methods at a large spatial scale. Parameterized methods require some readily available near-surface meteorological data (e.g., temperature and humidity) based on Stefan–Boltzmann's law (Liu et al., 2020; Niemelä et al., 2001). Parameterized methods are simple and computationally efficient but ancillary atmospheric parameters with high accuracy are not readily obtained globally (Cheng et al., 2019; Guo et al., 2019). Additionally, the global usage of parameterized methods is restricted because coefficients in most parameterized formulas were developed at a regional scale (Niemelä et al., 2001; Zhu et al., 2017). Hybrid methods suit global implementation because SLWR is directly derived from satellite TOA radiance based on extensive radiative-transfer simulation, which uses an off-line look-up-table or a regression model (Cheng et al., 2017; Wang et al., 2009; Wang et al., 2017; Tang and Li, 2008). However, hybrid methods are ineffective under cloudy-sky conditions because the satellite observations cannot provide the thermal contribution of clouds and the atmosphere below clouds (Wang et al., 2018; Yang and Cheng, 2020).

Machine learning (ML) is a powerful alternative for accurately retrieving global all-sky SLWR owing to its data-mining skills, strong adaptability, high nonlinearity, insensitivity to systematical biases of satellite observations, and high operating efficiency (Hao et al., 2019). ML methods have been successfully used to estimate SLWR in recent studies, such as the gradient boosting regression tree method (Wei et al., 2021), random forest (RF) method (Zhou et al., 2019), and artificial neural network model (Wang et al., 2012; Gharekhan et al., 2021). In recent years, deep learning exerted a stronger advantage in the field of environmental remote sensing compared with traditional ML methods (Yuan et al., 2020), benefiting from multi-layer architecture, big data, improved activation functions, and great power of hardware (Lecun et al., 2015; Shrestha and Mahmood, 2019). Bilgiç and Mert (2021) compared the performances of different methods in DLR estimation and

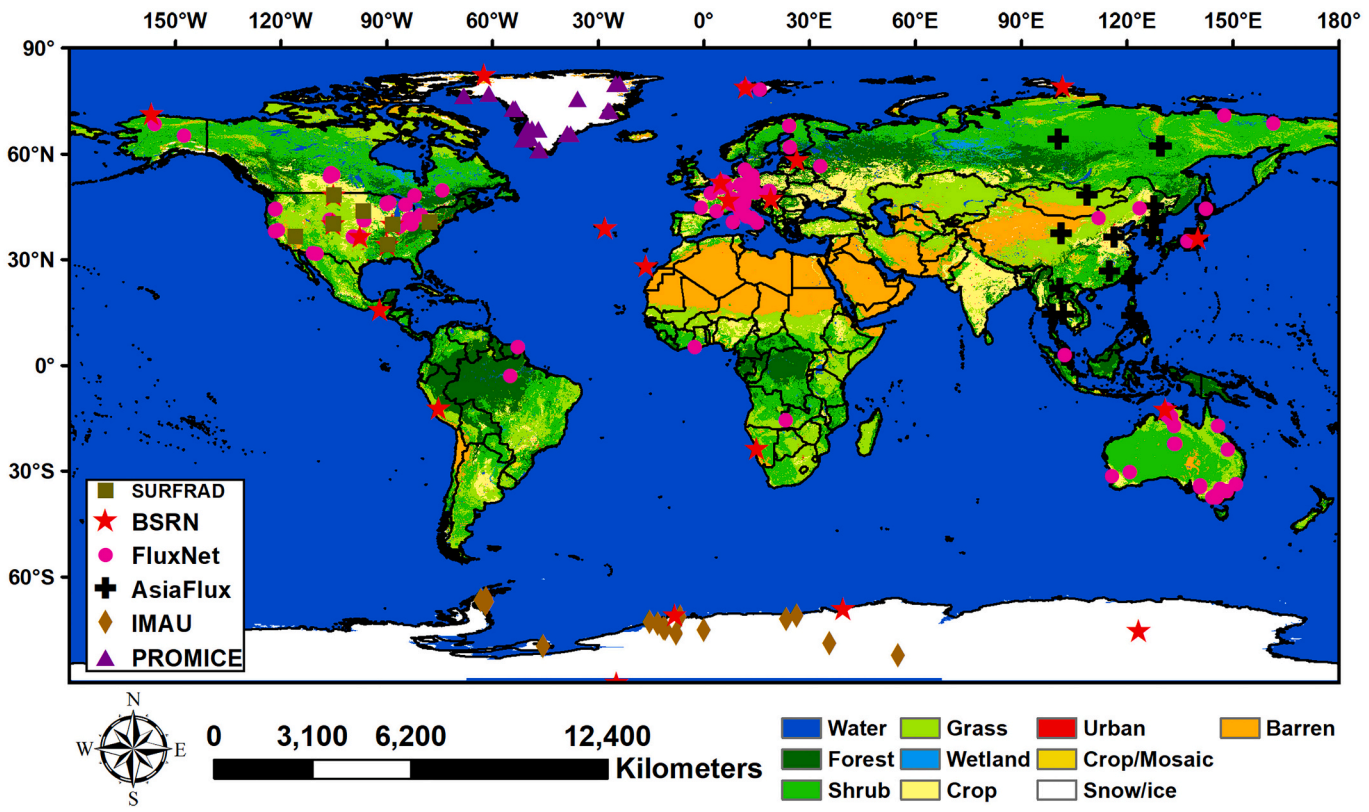

Fig. 1. Spatial distribution of global ground SLWR measuring stations. The base map is land cover according to the International Geosphere-Biosphere Programme (IGBP).

concluded that the deep neural network (DNN) outperformed other models. Zhu et al. (2021) used a novel DNN architecture to estimate DLR based on Himawari-8 brightness temperature (BT) on the Tibetan Plateau (TP) and showed better performance of the DNN compared with the RF and multi-layer perceptron (MLP). These studies revealed a great potential of DNNs with respect to estimating SLWR over regions with complex terrain and climatic conditions. However, except for the TP, more evaluations are needed to prove the ability of DNN in providing accurate estimates, flexible adjustment, and strong generalization under different surface and meteorological conditions, especially in polar regions with high cloud cover and low air temperature (T_a) at screen level (Zhang et al., 2008; Goosse et al., 2018).

The objective of this study was to develop an efficient and robust algorithm to estimate global, all-sky, spatiotemporally continuous daily mean SLWR (including DLR, ULR, and NLR) at a 0.05° resolution from AVHRR TOA observations and ERA5 near-surface meteorological variables. We aimed to (1) develop multiple densely connected convolutional neural network (DesCNN) models to estimate accurate all-sky SLWR over the globe. To avoid upscaling error of in situ measurements within an AVHRR footprint, the DesCNN models were trained using an integrated SLWR sample obtained from multiple SLWR products (Xiao et al., 2014; Jia et al., 2019; Baret et al., 2013; Wang et al., 2021a; Shang et al., 2021). It is difficult to retrieve global SLWR accurately under all conditions based only on a global DesCNN model owing to physical intrinsic limitations (Cheng et al., 2017) and the significantly non-uniform sample distribution (Guo et al., 2022). Transfer learning was used to further improve SLWR using limited samples at specific conditions (Yu et al., 2021; Li et al., 2022). (2) Utilize the DesCNN models to generate long-term, global SLWR datasets from the AVHRR TOA observations and ERA5 meteorological data. The generated daily mean SLWR dataset was evaluated using in situ measurements from different observational networks, such as the Surface Radiation Budget Network (SURFRAD (Augustine et al., 2000)), Baseline Surface Radiation Network (BSRN (Ohmura et al., 1998)), and FLUXNET (Wilson et al., 2002). An inter-comparison was conducted between AVHRR-based and three other SLWR products (CERES-SYN, GLASS-MODIS, and ERA5) under different surface and atmospheric conditions. The spatiotemporal consistency of AVHRR-based global SLWR was investigated using the CERES-SYN and ERA5 products. (3) Discuss the impact of each predictor in all-sky SLWR estimation, the contribution of TOA shortwave reflectance to DLR retrievals, the advantage of DesCNN models, and the idea of using instantaneous satellite observations to directly retrieve daily SLWR. Hereafter, our estimates derived from AVHRR and ERA5 data are named GLASS-AVHRR. To the best of our knowledge, this is the first study to use DesCNN models to estimate global SLWR from AVHRR observations. The rest of the study is organized in the following manner: Section 2 describes the data used in this study; Section 3 introduces the methods developed for estimating spatiotemporally continuous SLWR values; Section 4 presents the results; Section 5 depicts the contribution from AVHRR TOA reflectance; Section 6 provides a discussion; finally, Section 7 presents the conclusions.

2. Data

2.1. In situ observations

Ground-based SLWR observations from 2002 to 2018 were collected at 231 globally distributed sites (Fig. 1) to evaluate the capability of the DesCNN for estimating global SLWR: 24 sites belonged to the BSRN project (Ohmura et al., 1998; Wang and Dickinson, 2013), which uses Eppley Precision Infrared Radiometers and Kipp & Zonen CG 4 pyrometers to measure SLWR with an uncertainty of ±6% or 15 Wm^{-2} at the 95% confidence level (Wang and Dickinson, 2013). Seven sites belonged to Surface Radiation Budget Network (SURFRAD (Augustine et al., 2000)) and adopted the measurement standards of the BSRN project. The largest uncertainty for surface radiation measurements is ~2% for

pyrheliometers and ~ 5% for pyranometers (i.e., 15 Wm^{-2}). Twenty-six sites belonged to PROMICE, which monitors the Greenland ice sheet (Van As et al., 2011). The SLWR measurements were obtained using Kipp & Zonen CNR1 and CNR4 instruments with an expected accuracy of ±10% for daily totals (Fausto et al., 2021). Moreover, 129 sites belonged to FLUXNET (Wilson et al., 2002) and 29 to AsiaFlux (Yamamoto et al., 2005), for which longwave observations are measured using the Kipp & Zonen net radiometers (CNR1 or CNR1-lite) with uncertainty for CNR1 (or CNR1-lite) of ~10% at 95% confidence level for daily totals. Finally, 16 stations on the Antarctic peninsula belonged to the Institute for Marine and Atmospheric Research (IMAU (Kuipers Munneke et al., 2012)). These stations are equipped with Kipp & Zonen (K&Z) CNR1 net radiometers with factory-provided accuracy of the K&Z CG3 for daily SLWR totals of ±10% (Van Den Broeke et al., 2004). The land cover types of the above-collected sites include forests, croplands, grasslands, wetlands, shrublands, ice/snow, and barren land. The elevations of the sites vary from 2 to 3400 m. The latitudes of the sites range from the Equator to 90° and include different climate zones (i.e., tropical, dry, temperature, continental, polar, and alpine). Detailed information on every site is summarized in Table S1.

As in situ observations have different temporal resolutions, units, and storage forms, a strict data quality control was used to calculate daily mean values. For the networks officially providing daily SLWR observations, we directly used the observations by referencing the quality label (e.g., FLUXNET). For in situ measurements with a sub-daily sampling frequency (e.g., BSRN, SURFRAD), we adopted four steps for calculating daily mean SLWR measurements on a site-by-site basis, i.e., (1) checking and removing raw data records labeled with a bad quality flag; (2) calculating hourly mean values only if ≥ 90% of measurements were available during the hour; (3) calculating daily mean values only if 24 values were all available during a 24-h cycle; (4) checking temporal continuity and removing some unreasonable daily values by visual inspection and 3-σ rules. The NLR observations were calculated as the difference between the DLR and ULR components. These processing steps have been successfully applied in previous studies (Jia et al., 2018; Jiang et al., 2018; Chen et al., 2020) and ensure obtaining in situ measurements with good quality.

2.2. Satellite data products

2.2.1. AVH02C1

The AVHRR TOA observations (AVH02C1), including reflectance in the red (0.58–0.68 μm) and near-infrared (0.725–1.10 μm) regions and BT in the mid-infrared (3.55–3.93 μm) and two thermal-infrared (10.5–11.3 and 11.5–12.5 μm) spectral channels, were obtained from Version 5 of the land Long-Term Data Record (LTDR (Pedelty et al., 2007)). Using the best available data, the LTDR project generated a consistent AVHRR dataset that relies on eight AVHRR missions. The dataset includes observations from 1981 to the present and has a 0.05° × 0.05° spatial resolution and daily temporal resolution. To address the lack of onboard calibration for AVHRR visible to middle infrared bands, the LTDR applied a cross-calibration approach that relied on Terra MODIS data to fully characterize a stable invariant target for the cross-calibration of the AVHRR reflectance bands (Vermote and Saleous, 2006). The calibration accuracy was within 1% of MODIS data. Besides, a lock correction approach was proposed to mitigate the geolocation offset (Evans et al., 2010), which showed that the bias of the geolocation of AVHRR products was within two pixels. The quality of the AVHRR cloud mask also improved significantly and agreed with MODIS Aqua >90% (Franch et al., 2017). All of these improvements to the AVH02C1 facilitate the high accuracy and reasonable spatiotemporal variation of the long-term GLASS-AVHRR SLWR dataset.

2.2.2. CERES-SYN

CERES instruments on board the Terra, Aqua, and Suomi–National Polar-Orbiting Partnership satellites measure shortwave reflected radiation (0.3–5 μm), Earth-emitted thermal radiation (8–12 μm), and all wavelengths of radiation (0.3–200 μm), with 20-km spatial resolution at nadir (Wielicki et al., 1998). These CERES measurements are available at local equator crossing times of 10:30, 13:30, and 13:30 local time (LT), respectively. The CERES footprint radiance was convent instantaneous fluxes calculated using scene-dependent angular directional models (ADM) based on MODIS cloud retrievals (Loeb et al., 2003).

To estimate daily SLWR, two methods were adopted by the CERES project to account for diurnal fluctuations in longwave radiation between CERES measurements. The first method was a constant meteorology approach that assumes the cloud conditions at the time of satellite observation represent the conditions throughout the day (Doelling et al., 2013). The second incorporated contiguous geostationary satellite (GEO) imager-derived broadband fluxes to account for the diurnal variations of SLWR fluxes with a finer temporal resolution (Doelling et al., 2016), which has been adopted for the CERES-SYN product. CERES-SYN also includes in-atmosphere and surface fluxes using the Langley Fu-Liou RTM driven by CERES cloud profiles (Rutan et al., 2015a). Currently, CERES-SYN SLWR products are considered to be among the best surface flux products available (Gui et al., 2010; Tang et al., 2021; Dos Santos Nascimento et al., 2019).

2.2.3. GLASS-MODIS

GLASS-MODIS SLWR products, as part of the GLASS products suite (Liang et al., 2021a), include global instantaneous all-sky DLR, ULR, and NLR estimates at 1 km spatial resolution. Specifically, clear-sky ULR values were calculated using the general framework of the hybrid method to establish the linear and nonlinear relationships between clear-sky ULR and MODIS TOA radiances at three infrared channels (29, 31, and 32 (Cheng and Liang, 2016)). The cloudy-sky ULR was retrieved from the MODIS land surface temperature (MOD/Y06) and the GLASS broadband emissivity (Cheng et al., 2015) using Stefan–Boltzmann's law. For the clear-sky DLR product, a bulk formula (Guo et al., 2019) was used with the inputs of MODIS TOA radiance in channel 29, GLASS-MODIS clear-sky ULR, and MODIS water vapor (Cheng et al., 2017). A single-layer cloud model was subsequently applied to estimate cloudy-sky DLR values (Forman and Margulis, 2007). The daily SLWR was additionally calculated using a linear sine interpolation method from the GLASS-MODIS instantaneous SLWR products (Zeng and Cheng, 2021). A comprehensive assessment indicated the GLASS-MODIS instantaneous SLWR has comparable accuracy to existing SLWR products (Zeng et al., 2020).

Table 1
List of satellite-based and atmospheric reanalysis products used in this study.

Product name	Parameter	Spatial resolution	Temporal resolution	Download link
CERES-SYN	DLR, ULR, NLR	1° × 1°	Hourly	https://ceres.larc.nasa.gov/
GLASS-MODIS	DLR, ULR, NLR	1 km	Instantaneous/daily	http://www.glass.umd.edu/
ERA5	DLR, ULR, NLR, T_a, CWV, RH	0.25° × 0.25°	Hourly	https://www.ecmwf.int/
AVH02C1	Reflectance, BT, SZA, VZA, RAA	0.05° × 0.05°	Daily	https://ladsweb.modaps.eosdis.nasa.gov/

2.3. ERA5

Benefiting from developments in model physics, core dynamics, and data assimilation, ERA5 was produced in 2016 based on the Integrated Forecasting System (IFS) Cy41r2 with an enhanced horizontal resolution of 25 km and temporal resolution of 1 h compared with the previous ERA-Interim product (Hersbach et al., 2020). The ERA5 reanalysis product provides several types of data; for example, atmospheric

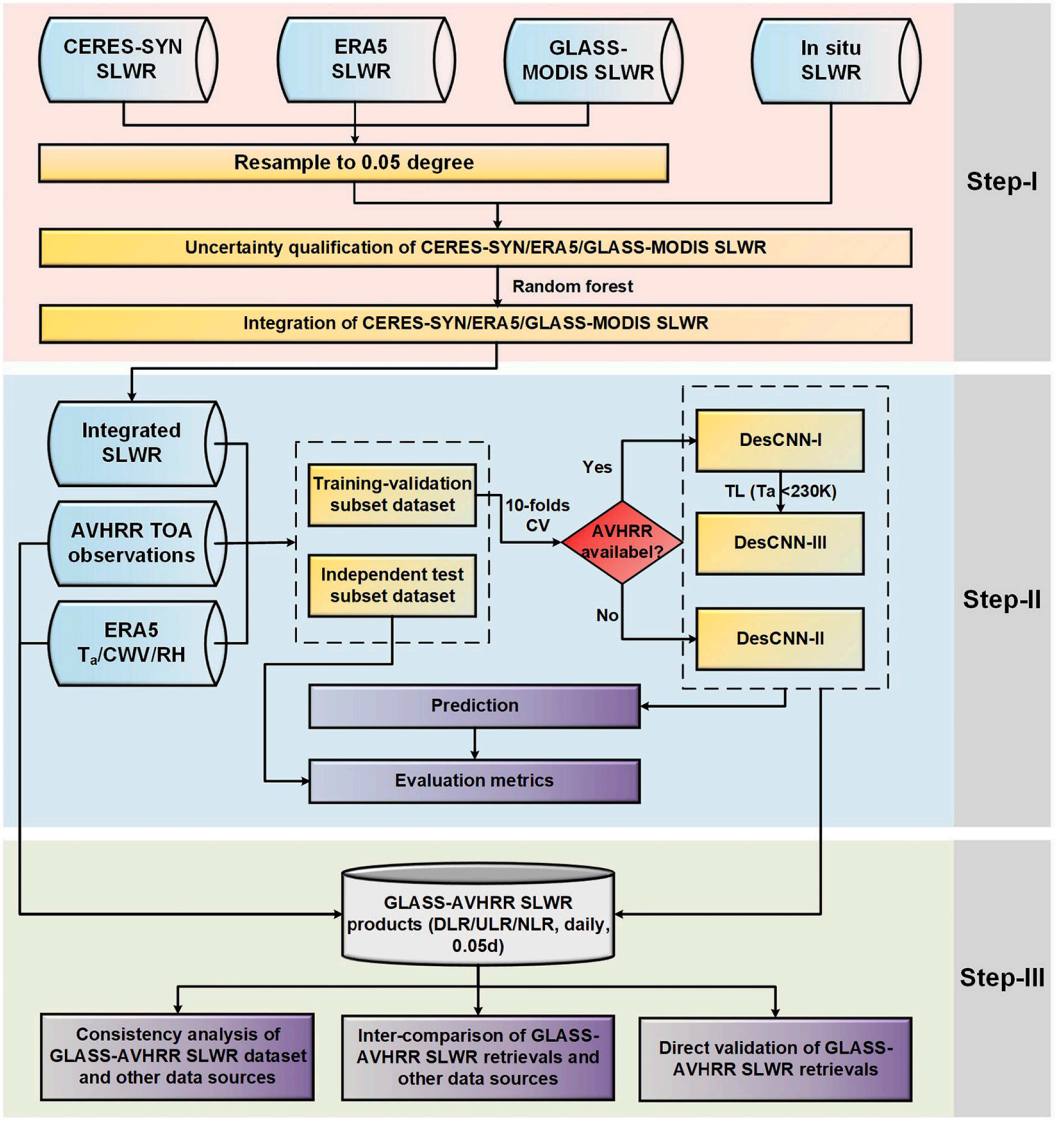

Fig. 2. Flowchart of the GLASS-AVHRR SLWR dataset generation using DesCNN models. The entire process consists of the generation of an integrated SLWR sample, the development and validation of the DesCNN models, and the production and evaluation of the GLASS-AVHRR SLWR products.

parameters at different pressure levels and surface single-level data. Several studies have evaluated the ERA5 SLWR data using regional or global in situ measurements (Letu et al., 2021; Zhu et al., 2021). The evaluations found the ERA5 SLWR, especially DLR, has high accuracy and outperforms CERES on average for hourly to monthly time scales over land (Tang et al., 2021). A summary of these products and their attributes is presented in Table 1.

3. Methods

The entire flow that uses DesCNN models to generate the spatio-temporally continuous GLASS-AVHRR SLWR products is shown in Fig. 2. The process roughly consists of three steps, i.e., integration of three SLWR products (Step-I), development and validation of the DesCNN models (Step-II), and production and evaluation of GLASS-AVHRR SLWR products (Step-III). Specifically, the CERES-SYN, ERA5, and GLASS-MODIS SLWR components were first resampled to 5 km resolution using the bilinear interpolation and area-weighting averaging methods, and the uncertainties of the three SLWR products were subsequently quantified using in situ measurements. Then the integrated SLWR sample between 2002 and 2018 was generated using the RF model over the globally distributed sites.

The integrated SLWR sample dataset was matched with AVHRR TOA observations [i.e., reflectance, BT, sun-viewing geometry (SZA, VZA, RAA)] and ERA5 meteorological parameters [including T_a, CWV, near-surface relative humidity (RH; 1000 hPa)], both spatially and temporally, to generate the training sample dataset for the DesCNN models. The training sample dataset was divided into two subsets, including a training and validation subset with a period from 2002 to 2015 and an independent test subset from 2016 to 2018. Three DesCNN models were developed based on the training and validation dataset using the 10-fold cross-validation method. Specifically, the DesCNN-I was used to retrieve SLWR estimates when the AVHRR TOA observations and ERA5 meteorological variables were all available. The DesCNN-II as a backup model for DesCNN-I was used to estimate SLWR values only using ERA5 meteorological variables to improve the spatial coverage of the GLASS-AVHRR products, especially before 2000. Additionally, the DesCNN-III as a supplementary model for DesCNN-I was developed using transfer learning, which was aimed to fine-tune the SLWR estimates when $T_a <$ 230 K.

After determining the DesCNN models, the GLASS-AVHRR SLWR products were produced and archived using the DesCNN models. The

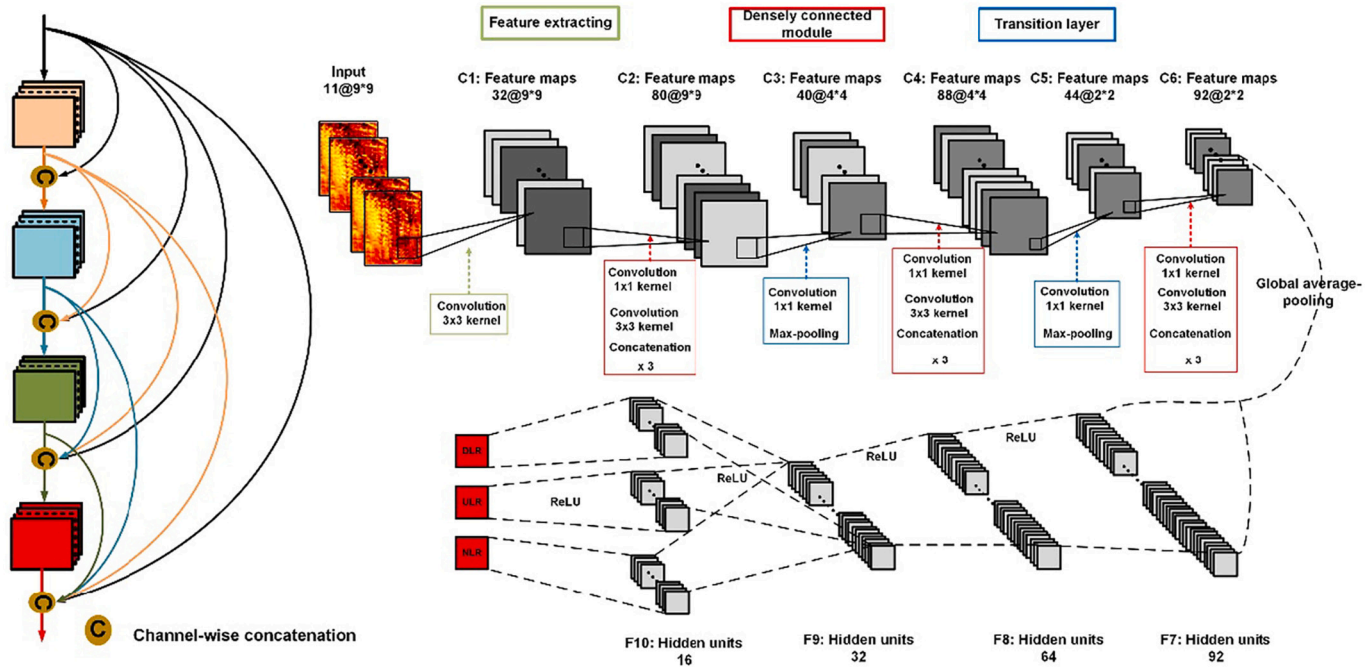

Fig. 3. End-to-end framework to derive mapping between AVHRR remote sensing images and SLWR samples. Inputs include AVHRR TOA observations, sun-viewing geometry, and ERA5 meteorological parameters. C1 ~ C6 are convolutional layers for performing feature engineering. F7 ~ F10 are fully connected layers that fit extracted feature maps to the integrated SLWR. The left panel shows the graphic structure of the densely connected layer.

GLASS-AVHRR SLWR products were then comprehensively evaluated using in situ measurements and the other three SLWR products (i.e., CERES-SYN, ERA5, and GLASS-MODIS). The evaluation mainly included three parts, i.e., direct validation of GLASS-AVHRR products against the in situ measurements, inter-comparison of SLWR estimates under different surface and meteorological conditions, and the spatiotemporal consistency analysis of the four SLWR products. A detailed description of each step is given below.

3.1. SLWR product integration

Determining high-quality samples for training the DesCNN models and validating the GLASS-AVHRR SLWR retrievals is a critical step. Currently, no algorithm and product can provide good SLWR estimates under all conditions (Jiao and Mu, 2022; Wang et al., 2021b). Several studies have shown that integrated retrievals generally have better accuracy and reliability based on some integration frameworks (Liang et al., 2018), such as Bayesian model averaging (BMA (Cheng et al., 2019)), multiresolution tree (MRT (He et al., 2013)), RF (Ma et al., 2020), and MLP (Wang et al., 2021a). To avoid increasing the uncertainty caused by the spatial representativeness error of in situ measurements within 5 km, the integrated sample dataset was treated as the 'real' values of SLWR to develop the DesCNN models.

CERES-SYN and ERA5 generally exhibit lower uncertainty in SLWR compared with other satellite-derived products and atmospheric reanalysis (Wang et al., 2021b; Wang and Dickinson, 2013; Tang et al., 2021; Gui et al., 2010). Additionally, GLASS-MODIS instantaneous SLWR products also show acceptable global accuracies with RMSEs of 18.15, 26.94, and 26.70 Wm^{-2} for clear-sky ULR, DLR, and NLR, respectively (Zeng et al., 2020). A multi-SLWR ensemble method based on the RF model was used to obtain more accurate and stable SLWR values by integrating CERES-SYN, ERA5, and GLASS-MODIS SLWR products at 5 km resolution. ERA5 meteorological variables (i.e., T_a, CWV, RH) were also fed into the RF model to enable the model to automatically determine the combination of SLWR retrievals most suited for specific scenarios (Wang et al., 2021a).

The prepared RF sample dataset was divided into two parts, i.e., a random 80% selection was used as a training dataset for driving the RF model and the remaining 20% served as the validation dataset to fine-tune the RF model. After determining the optimal model parameters, the trained RF model was used to generate the integrated SLWR sample dataset. The integrated SLWR dataset was subsequently used as the training sample to develop the DesCNN models. The uncertainties of the three original products and the RF-based integrated SLWR dataset are presented in Section 4.1.

3.2. DesCNNs development

3.2.1. End-to-end framework

Inspired by the superiority of densely connected neural networks (DenseNet) in four state-of-the-art DNN architectures (Huang et al., 2021; Zhu et al., 2021) (i.e., VGG (Sengupta et al., 2019), ResNet (He et al., 2016), Xception (Chollet, 2017), and DenseNet (Iandola et al., 2014)), the architecture of DenseNet was adopted to build the DesCNN models (Fig. 3) and then estimated the GLASS-AVHRR SLWR. Generally, the compelling advantages of DenseNet include alleviating the vanishing gradient problem, strengthening feature propagation, encouraging feature reuse, and reducing the number of parameters, all of which ensure comprehensive and deep training based on the integrated sample.

In a standard convolutional neural network (CNN) comprising L layers, the l^{th} layer normally reads the state from its preceding $l\text{-}1th$ layer based on the nonlinear transformation $H_l(\cdot)$, i.e., $x_l = H_l(x_{l\text{-}1})$, and then writes to the following $l + 1th$ layer. However, edge information in the feature maps is inevitably lost as the network becomes increasingly deep. To further improve information preservation and flow, the DenseNet structure was proposed (Fig. 3, left-panel). The l_{th} layer receives the feature maps from all of the preceding layers, $x_0, x_1, x_2, \ldots, x_{l\text{-}1}$, as inputs: $x_l = H_l([x_0, x_1, x_2, \ldots, x_{l\text{-}1}])$, and then passes them on to all subsequent $L\text{-}l$ layers (Huang et al., 2017). DenseNet requires fewer parameters than the standard CNN as there is no need to relearn redundant feature maps. Three dense blocks (C2, C4, and C6) were sequentially stacked to build the backbone of the DesCNN architecture.

DenseNet can use very narrow layers (i.e., a small number of feature

Table 2
Uncertainty statistics of the CERES-SYN, ERA5, GLASS, and the integrated SLWR components against in situ observations. Units of MBE and RMSE are Wm^{-2}.

Data set	DLR			ULR			NLR		
	R^2	RMSE	MBE	R^2	RMSE	MBE	R^2	RMSE	MBE
CERES	0.91	21.71	−2.18	0.95	18.17	−3.67	0.70	18.59	1.04
ERA5	0.93	21.95	−9.28	0.95	18.27	−1.90	0.71	19.87	−7.79
GLASS-MODIS	0.84	28.02	−4.53	0.95	17.77	−1.36	0.46	26.23	−3.41
Integrated	0.97	12.24	0.01	0.98	10.04	0.00	0.92	9.94	0.02

maps) to achieve favorable results because each layer in the network has received all preceding feature maps in the dense block. Therefore, the growth rate (i.e., the number of feature maps produced by H_l) was set to 32 in the DesCNN model. According to previous studies (He et al., 2016; Szegedy et al., 2016), a bottleneck layer composed of a 1×1 convolutional layer was used before a 3×3 convolutional layer to reduce the number of feature maps and improve the computational efficiency. A bottleneck layer was added behind each of the two dense blocks in the DesCNN architecture.

One issue worthy of note is that the size of feature maps does not change in the dense module; however, a standard CNN requires down-sampling layers that change the size of feature maps. To facilitate the down-sampling operation, transition layers (C3, C5) that perform convolution and pooling were inserted between dense blocks. The transition layers consist of batch normalization, rectified linear units (*ReLU*), a 1×1 convolutional layer, and a 2×2 maximum pooling layer. To improve model compactness, the m feature maps from the dense block are reduced to $\lfloor \theta m \rfloor$ at transition layers using the compression factor (θ (Huang et al., 2017)), which was assigned to be 0.5 at both the transition and bottleneck layers in this study.

Essentially, 9×9 image patches of predictors were fed into the input layer and 92 features were extracted from the consecutive convolutional layers (C1 ~ C6). These extracted features were then used as input to the fully connected layer to perform model fitting after the global averaging pooling operation. F7 ~ F10 is the fully connected layer for fitting features to SLWR by a large number of activation functions (*ReLU*). Three SLWR components were predicted in the output layer simultaneously based on the multi-task learning scheme. Therefore, the NLR was treated as an independent variable to be estimated, which avoids additional errors introduced from the estimated components.

3.2.2. Fine-tuning SLWR using transfer learning

To reduce the uncertainty of GLASS-AVHRR SLWR retrievals under specific conditions ($T_a \langle 230K$), transfer learning, which aims to transfer knowledge across domains (Zhuang et al., 2021), was used to resolve the systematical bias mainly caused by the non-uniform distribution of the sample dataset across the feature cube (Guo et al., 2022). The specific steps were as follows:

1) We determined the DesCNN-I in the source domain $D_s = \{(x,y)|\, x_i^s \in X_i^s, y_i^s \in Y_i^s, i = 1,\ldots,n_s, n_s \in N^+\}$ that included the features space X^s (AVHRR TOA observations, sun-viewing geometry, T_a, CWV, and RH) and global SLWR Y^s based on the spatiotemporally matched training sample dataset.
2) We retrained the modified DesCNN-III in the target domain $D_t = \{(x, y)|\, x_i^t \in X_i^t, y_i^t \in Y_i^t, X^t(T_a < 230K), i = 1,\ldots,n_t, n_t \in N^+\}$. Relying on the DesCNN-I architecture, the knowledge in D_s was transferred to improve the predictive performance of the DesCNN-III on D_t. Specifically, D_t was randomly divided into calibration and validation datasets (7:3 ratio). DesCNN-III replaced the last three layers of DesCNN-I with three new initialized layers to discover the knowledge on D_t, while other earlier layers kept the knowledge on D_s by freezing the weights. The calibration dataset was used to retrain the DesCNN-III to discover the specific patterns or relationships in D_t.
3) After the DesCNN-III model was retrained, the validation dataset was used to evaluate the performance of DesCNN-III on D_t. Based on transferring learning, the accuracy of GLASS-AVHRR SLWR retrievals under specific conditions ($T_a < 230$ K) can be improved significantly.

3.3. Training, evaluation, and analysis

SLWR sample datasets at all sites from 2002 to 2018 were compiled first, including predictors and the integrated SLWR sample. Usually, approximately two-thirds of samples are used to train models and the remaining one-third of samples are used for the validation of model retrievals. In this study, training and validation samples (918,323 records) from 2002 to 2015 were used to develop the DesCNN models, and the remaining samples (191,732 records) from 2016 to 2018 served as an independent test dataset. The entire training procedure consisted of three steps. (1) DesCNN-I & -II models were developed using the 10-fold cross-validation (CV) approach (Refaeilzadeh et al., 2009) based on the training and validation dataset. The entire training and validation dataset was equally divided into ten subsets and the model was trained using nine subsets and then validated with the remaining one subset. The procedure was repeated ten times to ensure that every subset was used to evaluate the model's performance. (2) After determining the hyper-parameter settings based on the 10-CV, the DesCNN-I & -II models were trained again using the entire training and validation dataset. The predictive power of the trained models was investigated using the independent test dataset to ensure the superiority and robustness of its predictive ability. (3) After completing the development of DesCNN-I & -II, DesCNN-III was developed using transfer learning as described in Section 3.2.2.

Three metrics were used to evaluate the accuracy of GLASS-AVHRR SLWR, including MBE, RMSE, and determination of coefficient (R^2). CERES-SYN, ERA5, and GLASS-MODIS SLWR products were used to evaluate the GLASS-AVHRR SLWR dataset under different surface and meteorological conditions against in situ measurements (386,721 records). The spatiotemporal consistency of GLASS-AVHRR SLWR products was evaluated at a global scale using the CERES-SYN and ERA5 products.

4. Results

4.1. Uncertainty quantification and integration of three SLWR products

Table 2 shows the accuracy statistics of the four SLWR datasets, including the CERES-SYN, ERA5, GLASS-MODIS, and the integrated SLWR sample. Benefiting from the introduction of GEO observations and assimilation of a large number of measurements, CERES-SYN and ERA5 SLWR estimates had higher R^2 and lower RMSEs compared with GLASS-MODIS. Specifically, CERES-SYN and ERA5 DLR and NLR showed higher accuracy, while the RMSE of GLASS-MODIS ULR had a marginal decrease (~0.5 Wm^{-2}). However, no product simultaneously provided three SLWR components with the best accuracy.

Compared with the other three products, the integrated SLWR values better correlated with in situ measurements. The integrated DLR showed small RMSE (12.24 Wm^{-2}) and MBE (0.01Wm^{-2}), at ~43.62% and 100% lower, respectively, than for CERES-SYN. For the integrated ULR, the RMSE (10.04 Wm^{-2}) and MBE (0.00 Wm^{-2}) were ~ 43.50% and 100% lower than those for GLASS-MODIS ULR. The most significant

Table 3
Results of 10-fold cross validation for the training and validation of SLWR retrievals against the integrated SLWR sample. Units of MBE and RMSE are Wm^{-2}.

Model	Variable	Training			Validation		
		R^2	RMSE	MBE	R^2	RMSE	MBE
DesCNN-I	DLR	0.98	10.14	−1.52	0.98	11.59	−3.35
	ULR	0.99	7.97	−0.82	0.99	9.47	−2.49
	NLR	0.90	9.87	−1.18	0.90	9.88	−1.26
DesCNN-II	DLR	0.97	12.26	1.99	0.97	12.96	−3.74
	ULR	0.99	9.40	−3.41	0.98	10.47	−3.57
	NLR	0.83	12.49	−0.03	0.84	12.23	−0.64

improvement was in the integrated NLR in comparison with CERES-SYN, with 46.53% and 98.07% lower RMSE and MBE, respectively. Therefore, the integrated SLWR dataset was treated as 'true' values and used to develop the DesCNN models.

4.2. Evaluation of model performance

4.2.1. Development of DesCNNs using the integrated SLWR dataset

The 10-fold CV results of DesCNN-I & -II in the training and validation dataset (2002–2015) are presented in Table 3. The training results were taken from the best fitting model over 10 CV rounds, while the validation results were obtained from the 10-round combination. For DesCNN-I, the ULR estimates presented the best training accuracy (R^2 = 0.99, RMSE = 7.97 Wm^{-2}, MBE = −0.82 Wm^{-2}). The training accuracy of DLR (NLR) estimates also performed well [R^2 = 0.98 (0.90), RMSE = 10.14 (9.87) Wm^{-2}, MBE = −1.52 (−1.18) Wm^{-2}]. Therefore, the overall training result of DesCNN-I was satisfactory for three SLWR components. Moreover, the validation accuracy of DesCNN-I was close to the training accuracy with small differences in R^2 (= 0), RMSE (< 2.5 Wm^{-2}), and MBE (< 1.8 Wm^{-2}). These statistics showed that the trained DesCNN-I model was robust and stable, and that no obvious overfitting occurred in the training procedure.

As a backup model, the DesCNN-II model would ensure the full coverage of the GLASS-AVHRR dataset to improve the data quality of the final dataset in light of the common gaps in the AVH02C1 product. Similarly, the performances of the DesCNN-II model between the training and validation phases were close to those of each other with negligible differences in R^2 (< 0.1), RMSE (< 0.7 Wm^{-2}), and MBE (< 2.74 Wm^{-2}), showing a good generalization in estimating the global SLWR. However, the training and validation accuracies were slightly lower than those of the DesCNN-I model, with a slight increase in RMSEs (1–3 Wm^{-2}). This is because cloud thermal properties implicitly provided by AVHRR TOA observations were not provided for the DesCNN-II model. Overall, the developed DesCNN-I & -II models were successful with high and comparable accuracy for estimated SLWR at both the training and validation phases. The quality assurance (QA) field was included in the archived GLASS-AVHRR SLWR products to distinguish the use of models.

With respect to investigating the predictive power, Fig. 4 shows the validation results of the DesCNN-I & -II models in the independent test dataset (2016–2018). SLWR retrievals from the DesCNN-I model agreed with the integrated samples (i.e., $R^2 \geq 0.89$) in the independent test dataset (Fig. 4a–c), with small RMSEs (9.66–10.01 Wm^{-2}) on average for SLWR estimates. The negative MBEs of estimated DLR (−2.85 Wm^{-2}) and ULR (−4.78 Wm^{-2}) indicated an underestimation, which mainly occurred in the high SLWR values.

The performance of DesCNN-II in the independent test dataset was satisfactory for the three SLWR components (Fig. 4d–f) with R^2 of 0.84–0.99, RMSEs of 10.71–12.94 Wm^{-2}, and MBEs of −0.92–-5.77 Wm^{-2}. This demonstrated that DesCNN-II provided SLWR estimates with an acceptable uncertainty and was a good backup model for estimating the global SLWR. The accurate performances for the independent test dataset illustrated that the DesCNN-I & -II models had a strong predictive power, i.e., the potential to generate a long-term spatially

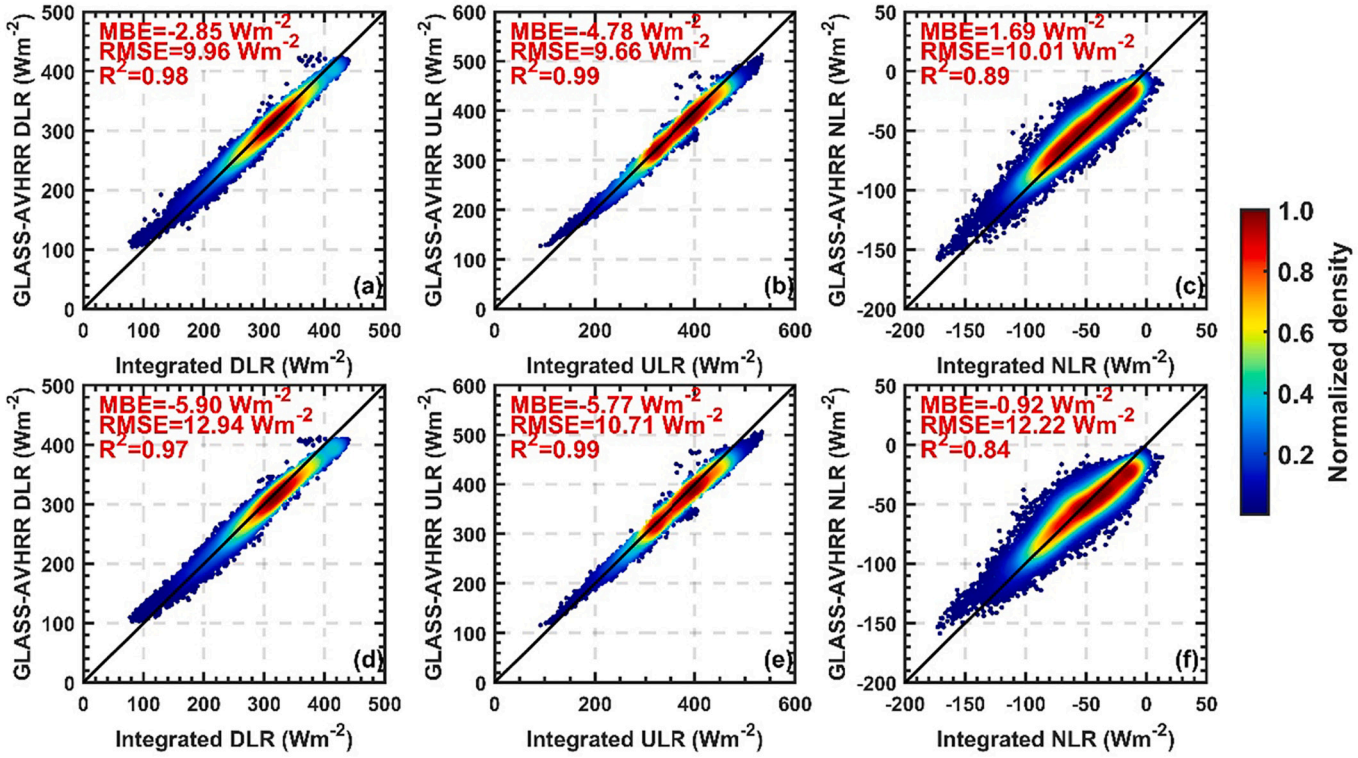

Fig. 4. Evaluation of GLASS-AVHRR SLWR estimates in the independent test dataset against the integrated SLWR values. Resulting (a–c) DesCNN-I and (d–f) DesCNN-II models. Solid lines denote 1:1 lines. MBE, RMSE, and R^2 are given. Units of MBE and RMSE are Wm^{-2}. The colour bar represents the normalized density of the samples, which was calculated using a Gaussian kernel density function.

Table 4
Evaluation of the GLASS-AVHRR SLWR retrievals at $T_a < 230$ K using the DesCNN-I&III models against the integrated SLWR sample. Units of MBE and RMSE are Wm^{-2}.

Variable	DesCNN-I			DesCNN-III		
	R^2	RMSE	MBE	R^2	RMSE	MBE
DLR	0.52	21.49	18.77	0.55	10.49	2.02
ULR	0.87	20.36	19.51	0.89	5.09	−1.56
NLR	0.30	10.91	−2.15	0.47	10.71	4.08

continuous SLWR dataset.

The DesCNN-III model was additionally developed based on transfer learning to correct the systematical bias of DesCNN-I at $T_a < 230$ K. Table 4 shows a comparison of SLWR estimates derived from the DesCNN-I & -III models in the independent test dataset. The DesCNN-III model mainly improved the accuracies of the DLR and ULR components. An obvious overestimation under low T_a conditions was well resolved, i.e., MBEs decreased by ~16 and 18 Wm^{-2} for DLR and ULR, respectively. The RMSEs of SLWR estimates also decreased significantly by 51.19% for DLR and 75% for ULR, respectively. However, the improvement in NLR retrievals was not significant (RMSE only decreased by 0.2 Wm^{-2}). Generally, the DesCNN-III model greatly strengthened the performance of the SLWR retrievals at $T_a < 230$ K, further improving the overall accuracy of the SLWR estimates.

4.2.2. Spatiotemporal validation using in situ observations

To investigate whether these models could generate long-term spatiotemporally continuous SLWR datasets with high accuracy, the spatial-temporal performances of the DesCNN models was evaluated using globally distributed in situ measurements. Fig. 5 shows the spatial performance of DesCNN models with respect to estimating the SLWR. For the DLR estimates (Fig. 5a, d, g), DesCNN models performed well in the U.S., Europe, and Australia (RMSEs <20 Wm^{-2}, $R^2 > 0.8$). However, there were relatively large uncertainties for eastern Asia at some sites (RMSE >25 Wm^{-2}, $R^2 < 0.8$). Previous studies reported that systematic errors and operation-related problems were common in the radiation measurements obtained in China (Zhang et al., 2015; Tang et al., 2010; Shi et al., 2008). The large uncertainty of DLR retrievals from eastern Asia was likely attributable to the poor quality of the in situ measurements. Compared with the DLR retrievals, the overall uncertainty of ULR values was lower (RMSEs <15 Wm^{-2}; Fig. 5e). The ULR estimates at most sites correlated well with the in situ measurements ($R^2 > 0.9$; Fig. 5b). However, significantly negative MEBs (< −8 Wm^{-2}) of DLR and ULR estimates were observed in tropical areas, mainly in Australia (Fig. 5g, h), which was corresponding to the underestimation at high values (Fig. 4). The reason for the underestimation is mainly due to the smaller sample size in tropical areas (Fig. S2), which results in a local overfitting issue. In contrast, the uncertainty of the estimated NLR ($R^2 <$ 0.8, RMSEs <25 Wm^{-2}; Fig. 5c, f) was generally larger than that of the DLR and ULR, although the MBEs of the NLR estimates were overall

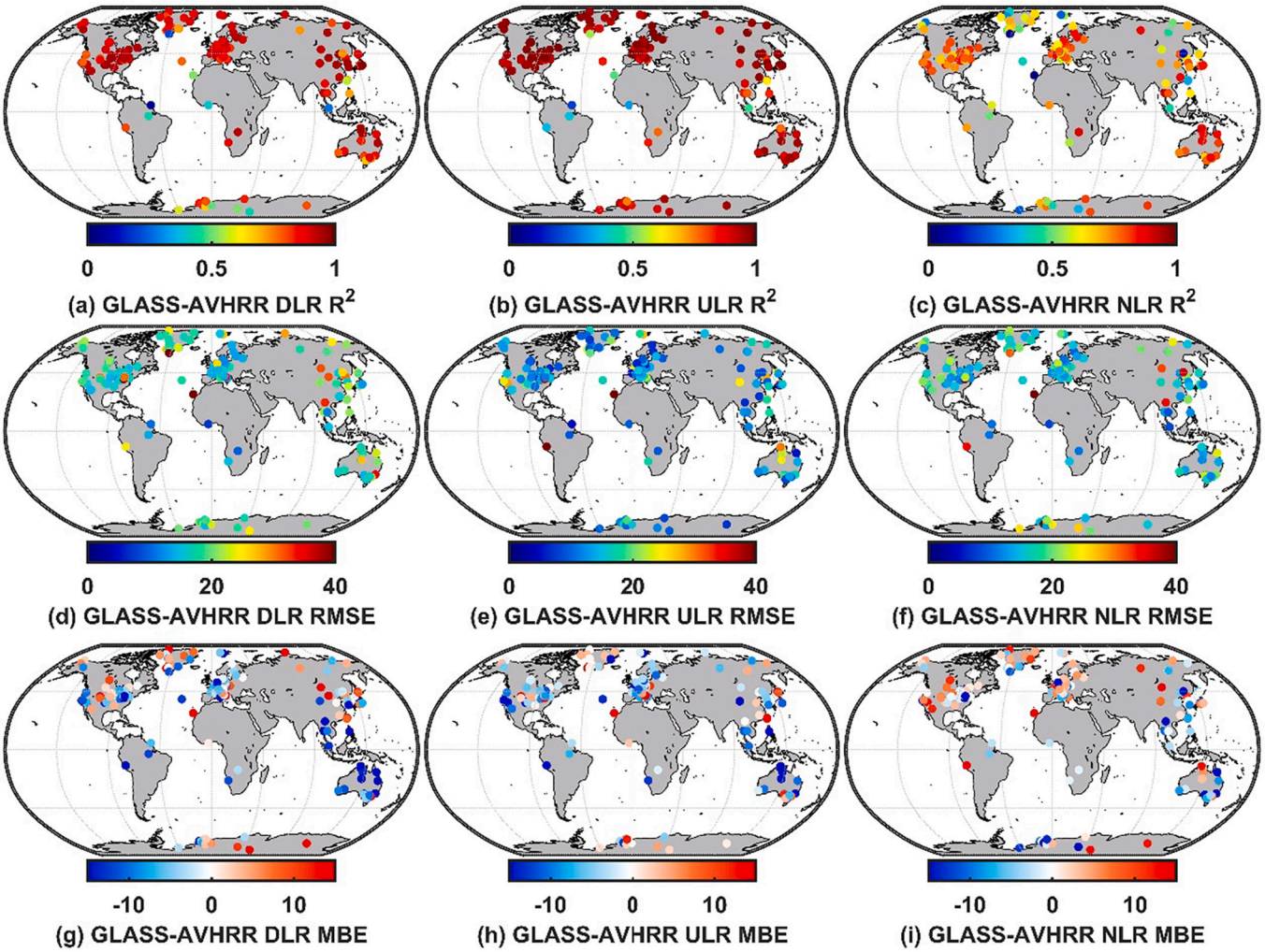

Fig. 5. Spatial distribution of statistic metrics. (a–c) R^2, (d–f) RMSE, and (g–i) MBE of daily GLASS-AVHRR SLWR at each meteorological station between 2002 and 2018. (a, d, g) are validation results of DLR; (b, e, h) are validation results of ULR; (c, f, i) are validation results for NLR.

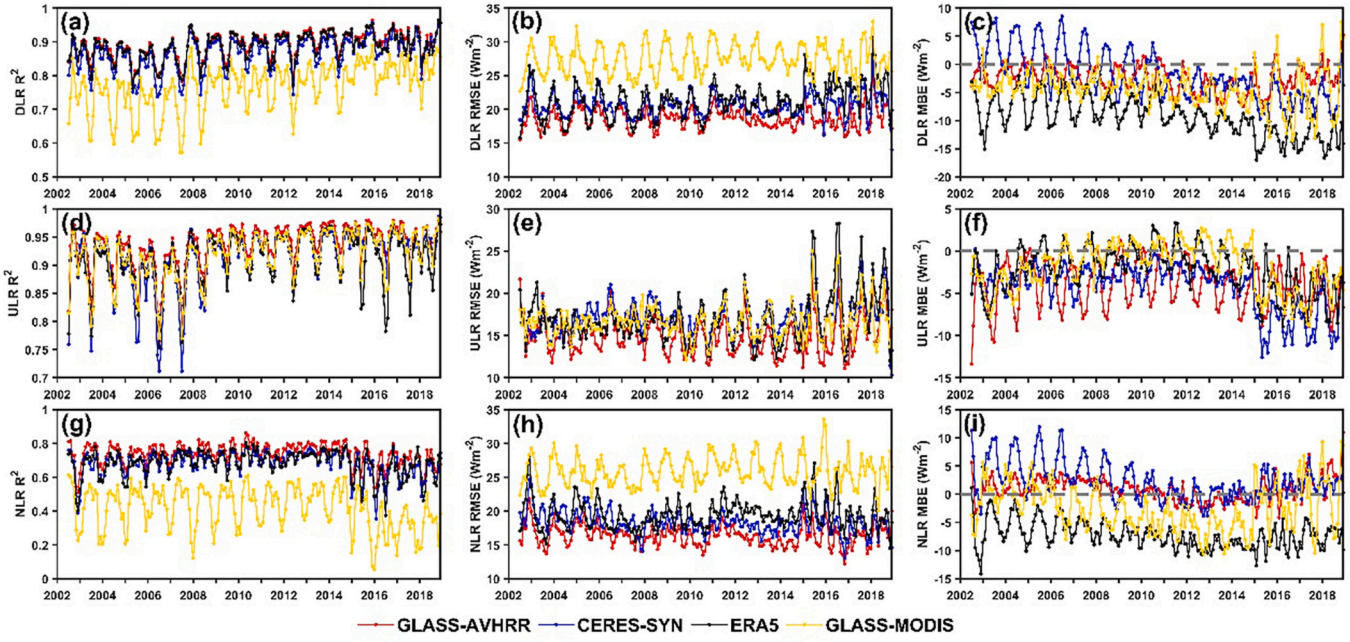

Fig. 6. Temporal profiles of R^2, RMSE, and MBE of the global daily mean SLWR. The profiles based on (a–c) DLR, (d–f) ULR, and (g–i) NLR retrievals as a function of the month between 2002 and 2018. The red line denotes values from GLASS-AVHRR, the blue line denotes values from CERES-SYN, black line denotes values from ERA5, and the yellow line denotes values from GLASS-MODIS. (For interpretation of the references to colour in this figure legend, the reader is referred to the web version of this article.)

smaller. The larger uncertainty of NLR was attributed to the fact that the NLR is comprehensively affected by surface and atmospheric thermal properties but DLR and ULR are more dependent on atmospheric and surface thermal properties, respectively. Overall, the DesCNN models successfully estimated the SLWR at a global scale, while its performance was slightly reduced in tropical and polar regions.

Fig. 6 shows the temporal performance of the DesCNN models for estimating SWLR at all monitoring sites as a function of the month of the year between 2002 and 2018. The temporal robustness of the model was well maintained over the entire period (Fig. 6a, d, g), with $R^2 > 0.8$ for DLR and ULR, and > 0.6 for NLR, generally higher than those of other products. Stable and smaller RMSEs of the GLASS-AVHRR SLWR retrievals were observed over the entire period (Fig. 6b, e, h). In addition, GLASS-AVHRR DLR and NLR estimates showed smaller MBEs over the entire period compared with the other three products (Fig. 6c, j), while the GLASS-AVHRR ULR values had a larger fluctuation of MBE (Fig. 6f). Interestingly, the correlation had an overall concave-upward or downward parabolic trend in each year for SLWR estimates, which was grossly proportional to annual variations in atmospheric temperature and moisture profiles dominated by solar radiation heating.

One issue worthy of note was that there were larger uncertainties from 2015 to 2018 than from 2002 to 2014 in the four SLWR datasets. The large uncertainties from 2015 to 2018 were due to the unevenly distributed sites and varying observation lengths at every site rather than the models themselves. Fig. S1 shows the lengths of available observations at every site. Most in situ observations after 2015 were taken from the PROMICE and IMAU networks located in the polar regions. The larger uncertainty of SLWR values in the poles resulted in larger RMSEs after 2015. Generally, compared to the other three products, the DesCNN models showed temporal superiority and robustness with respect to estimating SLWR, which demonstrated the potential to accurately reconstruct the long-term global SLWR variation.

4.3. Comparison with other products

Fig. 7 shows the direct validation results of the four SLWR datasets against globally distributed in situ measurements. GLASS-AVHRR SLWR retrievals had better agreement with in situ observations compared with the other three products (Fig. 7d, h, l). Specifically, the GLASS-AVHRR DLR retrievals explained 92% variation of in situ DLR measurements, and had the highest accuracy (RMSE = 18.66 Wm^{-2}, MBE = −2.69 Wm^{-2}), followed by CERES-SYN, ERA5, and GLASS-MODIS. GLASS-AVHRR ULR retrievals were also best correlated with in situ measurements among the four datasets ($R^2 = 0.96$). The other three products showed similar and comparable accuracies for their ULR values. For NLR, GLASS-AVHRR exhibited a higher accuracy (RMSE = 16.29 Wm^{-2}, MBE = 0.49 Wm^{-2}) than CERES-SYN, ERA5, and GLASS-MODIS. Generally, the GLASS-AVHRR dataset showed lower uncertainty when compared with the other three well-known SLWR products. However, the underestimation of the GLASS-AVHRR at high values (DLR > 400 Wm^{-2}, ULR > 500 Wm^{-2}) is worthy of more attention.

To more clearly reveal the uncertainty variation of GLASS-AVHRR SLWR estimates, the four datasets were comprehensively evaluated under the different surface and meteorological conditions, including elevation, land cover type, T_a, CWV, and RH, in different latitudinal zones (i.e., polar regions at latitudes >60° and non-polar regions at latitudes <60°). GLASS-AVHRR DLR estimates had smaller uncertainties than those of the other three products at most altitude ranges (Fig. 8a, b), with the largest RMSEs of 26.58 and 22.38 Wm^{-2} for non-polar and polar regions, respectively. Meanwhile, most MBEs of GLASS-AVHRR DLR were closer to zero compared to other products at different latitude bins. As the altitude increased, the RMSEs and MBEs of the DLR estimates increased, which is likely due to the decreasing sensitivity of DLR to variations in cloud cover and water vapor (Naud et al., 2013). For most land cover types (Fig. 8c, d), GLASS-AVHRR DLR estimates exhibited lower uncertainties, particularly for forest, wetland, and snow surfaces, with RMSEs of 15.43 (19.29), 21.31 (19.78), and 20.50 Wm^{-2} in polar (non-polar) regions. However, the uncertainty of GLASS-AVHRR DLR was larger than that of the other products in cropland (latitudes >60°).

For different meteorological conditions, the GLASS-AVHRR DLR dataset also exhibited an obvious advantage with respect to uncertainty variation. GLASS-AVHRR DLR estimates had the smallest RMSEs and MBEs throughout the whole T_a range (Fig. 8e, f), with RMSEs of

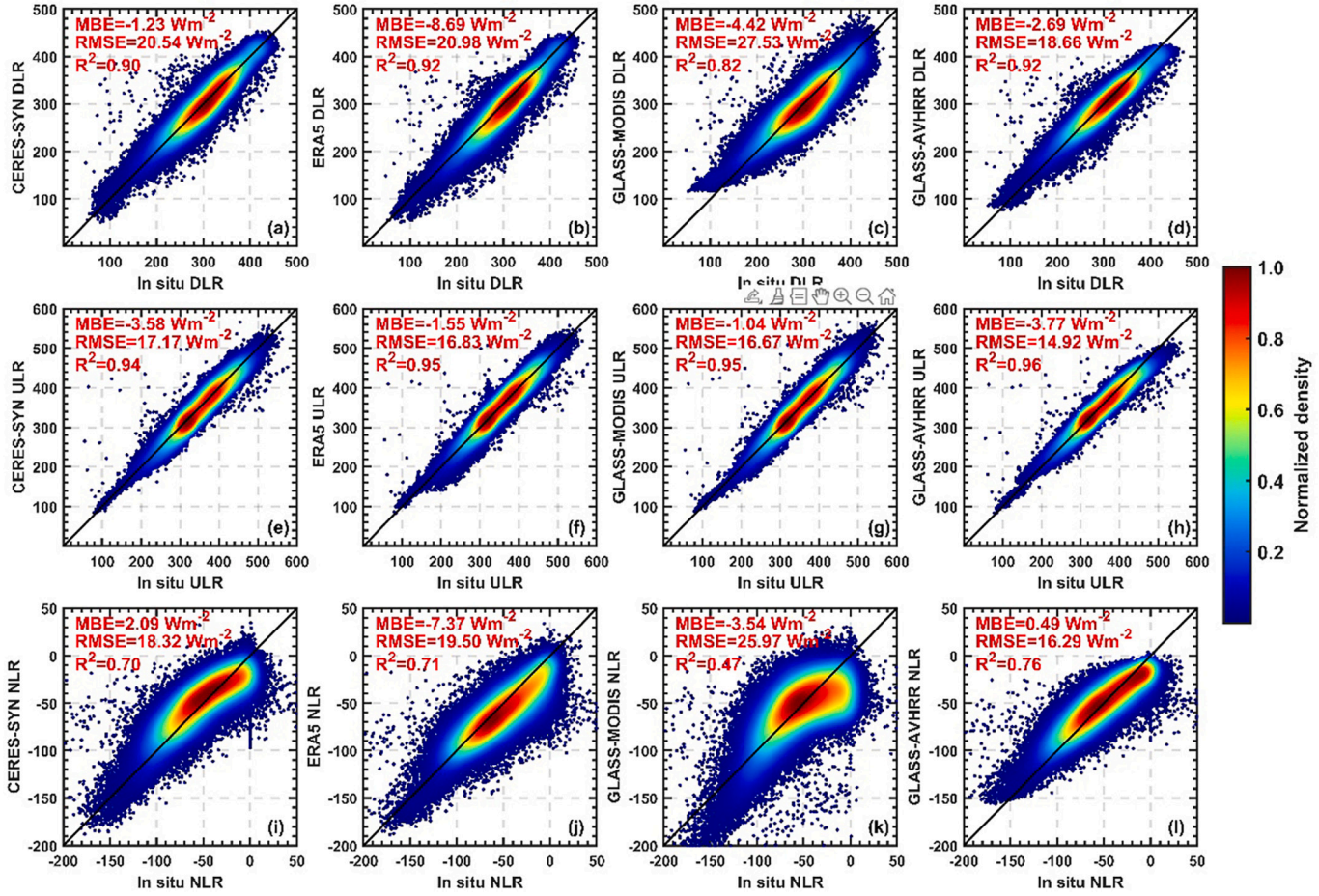

Fig. 7. Evaluation of daily SLWR values from the CERES-SYN, ERA5, GLASS-MODIS, and GLASS-AVHRR datasets. Results for (a–d) DLR, (e–h) ULR, and (i–l) NLR. Solid lines denote 1:1 lines. The MBE, RMSE, and R^2 are given. The colour bar represents the normalized density of samples, calculated using a Gaussian kernel density function.

17.66–27.30 Wm^{-2} (16.09–23.41 Wm^{-2}) for non-polar (polar) regions. Most biases were closer to zero, with MBEs varying from 5 to −3 Wm^{-2} for polar and non-polar regions. However, when CWV > 40 $kg.m^{-2}$, the error of GLASS-AVHRR DLR estimates was larger than that of CERES-SYN and ERA5 for non-polar regions (Fig. 8g). The differences in RMSE between GLASS-AVHRR and ERA5 DLR values ranged from 1 to 3 Wm^{-2}. The larger uncertainty at CWV > 40 $kg.m^{-2}$ was caused by the underestimation (MBE < −8 Wm^{-2}; Fig. 5g) of GLASS-AVHRR DLR estimates at high values (> 400 Wm^{-2}; Fig. 7). The fewer samples in the tropical areas and the decreasing sensitivity of DLR to high CWV (Ruckstuhl et al., 2007) are responsible for the underestimation of GLASS-AVHRR DLR. At other CWVs and RHs, the GLASS-AVHRR DLR estimates still showed smaller RMSEs and MBEs than the other datasets for both non-polar and polar regions (Fig. 8h, i, j).

The uncertainty variations of regional ULR and NLR estimates at different surface and meteorological conditions are presented in Figs. S3 and S4. GLASS-AVHRR ULR and NLR estimates exhibited pronounced advantages with respect of accuracy over the other three products for most surface and meteorological conditions. However, it is worth noting that GLASS-AVHRR ULR at CWV > 48 $kg.m^{-2}$ was worse than the other three products. The largest difference in RMSE was ~4 Wm^{-2}, which was observed between GLASS-AVHRR and ERA5 ULR values at a CWV of 56–64 $kg.m^{-2}$, which was also caused by the underestimation (MBEs < −8 Wm^{-2}; Fig. S3g) of GLASS-AVHRR ULR at high values (Fig. 7) in tropical regions (Fig. 5h). Overall, the GLASS-AVHRR SLWR products were better than those of the current state-of-art SLWR products at the most surface and meteorological conditions. However, more effort is needed to address the underestimation in GLASS-AVHRR DLR and ULR estimates in tropical areas when atmospheric CWV is >40 $kg.m^{-2}$.

4.4. Generation of global SLWR products

The major advantages of using polar-orbiting AVHRR observations to estimate SLWR are the near-complete coverage of the Earth at a daily scale and a long duration, i.e., from 1981 to the present, which ensures the generation of a long-term global seamless GLASS-AVHRR SLWR dataset. CERES-SYN SLWR maps were used to investigate the spatial consistency of the GLASS-AVHRR SLWR retrievals. Fig. S5 shows the global spatial distribution of GLASS-AVHRR and CERES-SYN SLWR values in January 2008. The monthly global SLWR estimates were similar between the CERES-SYN and GLASS-AVHRR products, with a DLR of 239.42 ± 86.29 Wm^{-2}, ULR of 287.98 ± 95.35 Wm^{-2}, and NLR of −49.37 ± 23.16 Wm^{-2} for GLASS-AVHRR and DLR of 234.77 ± 94.42 Wm^{-2}, ULR of 287.32 ± 102.04 Wm^{-2}, and NLR of −52.55 ± 26.47 Wm^{-2} for CERES-SYN. Spatially, DLR and ULR values were high in South America, southern Africa, and Australia in January (Fig.S5a, b), while high NLR values occurred in northern Eurasia, Greenland, and central South America (Fig. S5c). A similar latitudinal distribution of SLWR estimates was reported for the two datasets from January (Fig. 9g–i). A better agreement between GLASS-AVHRR and CERES-SYN SLWR was observed at latitudes between 0° and 40° N. However, a larger discrepancy occurred from −20° to −40°, especially in Australia, which was mainly due to the local overfitting issue of the DesCNN models (induced by the sparsely distributed sites in tropical areas).

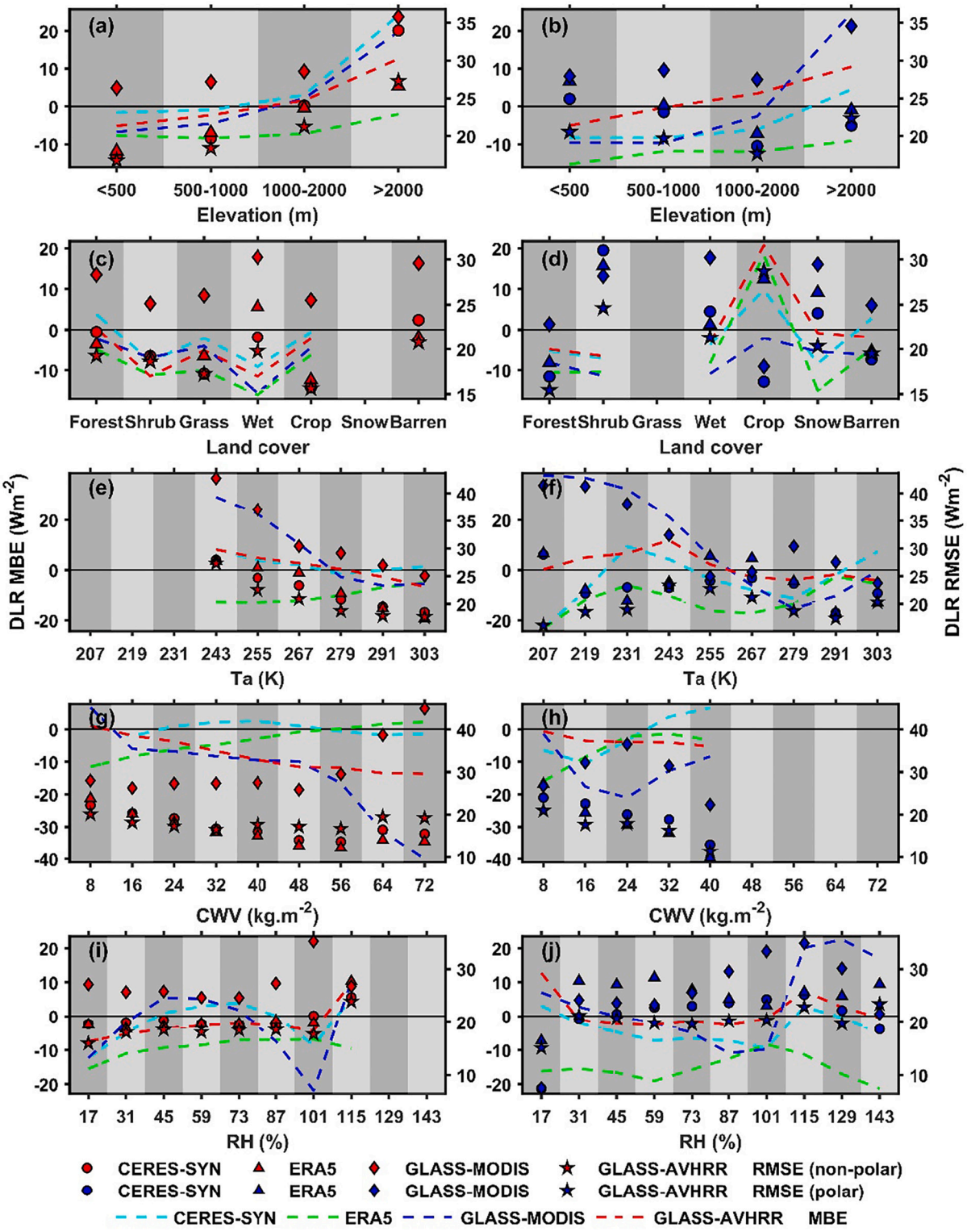

Fig. 8. Uncertainty variations (RMSE, MBE) of CERES-SYN, ERA5, GLASS-MODIS, and GLASS-AVHRR DLR retrievals for polar and non-polar regions under different conditions. Uncertainty variation as a function of (a–b) elevation, (c–d) land cover, (e–f) T_a, (g–h) CWV, and (i–j) RH. Red markers denote results from non-polar regions, and blue markers denote results from polar regions. The dashed lines represent the MBE variations of the DLR values from the four datasets under different surface and meteorological conditions. (For interpretation of the references to colour in this figure legend, the reader is referred to the web version of this article.)

As the sun crosses the equator, high SLWR values from the two datasets occurred in the Northern Hemisphere in July (Fig. S6). The monthly global GLASS-AVHRR estimates were 283.39 ± 103.02 Wm^{-2} for DLR, 336.96 ± 121.42 Wm^{-2} for ULR, and − 54.92 ± 29.40 Wm^{-2} for NLR; for CERES-SYN products, these values were 288.83 ± 111.62 Wm^{-2} for DLR, 337.99 ± 131.95 Wm^{-2} for ULR, and − 49.16 ± 33.11 Wm^{-2} for NLR. Similar latitudinal distributions of GLASS-AVHRR and CERES-SYN SLWR estimates were observed (Fig. 9j–l). GLASS-AVHRR SLWR was slightly larger than the CERES-SYN for Greenland and Antarctica in July (Fig. 9d–e).

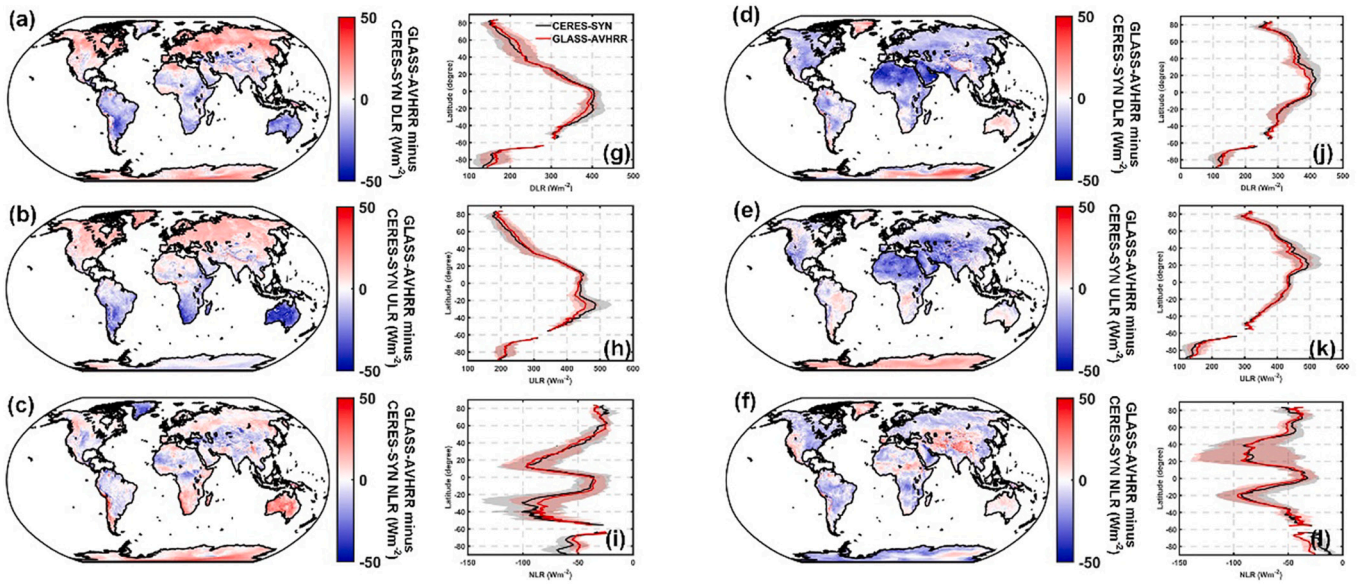

Fig. 9. Global differences between GLASS-AVHRR and CERES-SYN SLWR estimates. Estimates at a monthly time scale (a–f), and the corresponding comparison of latitudinal gradients between the two datasets (g–l). The left panels (a–c, g–i) show the results from January 2008; the right panels (d–f, j–l) show the results from July 2008. Positive values (red) indicate that the GLASS-AVHRR estimates are larger. Shading represents the variation in the SLWR values. (For interpretation of the references to colour in this figure legend, the reader is referred to the web version of this article.)

We further calculated the global mean SLWR values of GLASS-AVHRR and CERES-SYN products in overlapping land pixels for each month in 2008 (Table S2). We found that GLASS-AVHRR SLWR estimates were close to those of CERES-SYN. The differences in SLWR between the two datasets were the smallest in winter (~0–2 Wm^{-2}), while the largest differences occurred in summer (difference of ~5 Wm^{-2}). Therefore, the GLASS-AVHRR and CERES-SYN SLWR products had a good spatial consistency across the globe based on the above statistics, a phenomenon that confirmed the ability of DesCNN models to accurately estimate the global SLWR.

Long-term variations in global SLWR based on the GLASS-AVHRR are presented in Fig. 10. Temporal variations in the differences between zonal mean daily SLWR estimates between GLASS-AVHRR and CERES-SYN and between GLASS-AVHRR and ERA5 overland from 1981 to 2018 are also included. An obvious annual pattern driven by the course of the sun's position was apparent in DLR and ULR. A higher intensity of NLR was observed in the tropical ($0 \pm 15°$) and polar areas ($> \sim 50°$), reflecting more cloud covers in the poles and higher water vapor content in the tropical zone (King et al., 2013; Eastman and Warren, 2013). In addition, differences were small overall, demonstrating that GLASS-AVHRR SLWR products were consistent with CERES-SYN after 2000 and with ERA5 from 1981 to 2018, both spatially and temporally. There was a systematic underestimation in tropical areas for DLR and ULR (compared with CERES-SYN and ERA5), which has been described in Section 4.3. There are several reasons for these spatiotemporal differences, including differences in spatial resolution, driving data uncertainties, sensor channel responses, and particularly, retrieval algorithms. Overall, GLASS-AVHRR products had a higher spatial resolution (5 km), a longer period (1981–2018), and lower overall uncertainty (Fig. 7) compared with the current state-of-the-art SLWR products. As such, GLASS-AVHRR has the potential to play an important role in numerical simulations and climate trends analysis.

5. Contribution of the TOA reflectance to the all-sky DLR

The selection of proper input features is a prerequisite for DesCNN models to estimate accurate GLASS-AVHRR SLWR retrievals. Satellite TOA radiances comprehensively record thermal radiation information on the surface and atmospheric column under clear-sky conditions; thus, clear-sky SLWR can be retrieved from satellite thermal observations by establishing regression relationships (Cheng and Liang, 2016; Wang and Liang, 2009). However, when clouds are present, the DesCNN models cannot estimate accurate SLWR from satellite TOA radiances as the longwave radiation emitted from the surface and atmosphere below the clouds is dramatically absorbed by low-level liquid water clouds (Wang et al., 2018; Yang and Cheng, 2020).

For cloudy-sky conditions, DLR consists of two parts, i.e., atmospheric longwave radiation below the clouds and cloud-emitting longwave radiation toward the surface. As the thermal radiation emitted by the near-surface atmospheric gases is absorbed by the low-level clouds, ERA5 near-surface meteorological parameters was used to help estimate the atmospheric longwave radiation below the clouds. According to the Stefan–Boltzmann equation, T_a and atmospheric effective emissivity (ε_a) derived from RH and T_a are needed to calculate the near-surface atmospheric longwave radiation. Additionally, considering water vapor as the most important greenhouse gas for longwave radiation, CWV was used to retrieve atmospheric longwave radiation below the clouds. Therefore, T_a, RH, and CWV were determined to help retrieve DLR below the clouds.

For retrieving cloud-emitting longwave radiation, ε_a was revised by introducing cloud fraction (CF) to consider cloud influence on the DLR in previous studies (Crawford and Duchon, 1999; Yang et al., 2010; Carmona et al., 2014). Some studies have employed CF to derive the all-sky DLR (Lopes et al., 2022) and produced the all-sky longwave radiation product (Karlsson et al., 2013). CF can be alternatively represented by the ratio of downward shortwave radiation (R_{sw}) and its clear-sky value. Therefore, R_{sw} has been directly used to characterize cloud information in developing ML methods to estimate the all-sky DLR (Wei et al., 2021; Feng et al., 2020). Considering that uncertainty in R_{sw} estimates impacts the estimated DLR, we used raw TOA shortwave reflectance to provide indications of atmospheric and cloud properties in this study. By incorporating AVHRR TOA reflectance (characterizing clouds properties), BTs and near-surface meteorological information provided by ERA5, we expected that DesCNN models could more accurately estimate all-sky DLR retrievals.

Table 5 presents the evaluation results of GLASS-AVHRR SLWR retrievals using different input features to understand their contributions to estimating GLASS-AVHRR SLWR. The worst accuracy of GLASS-

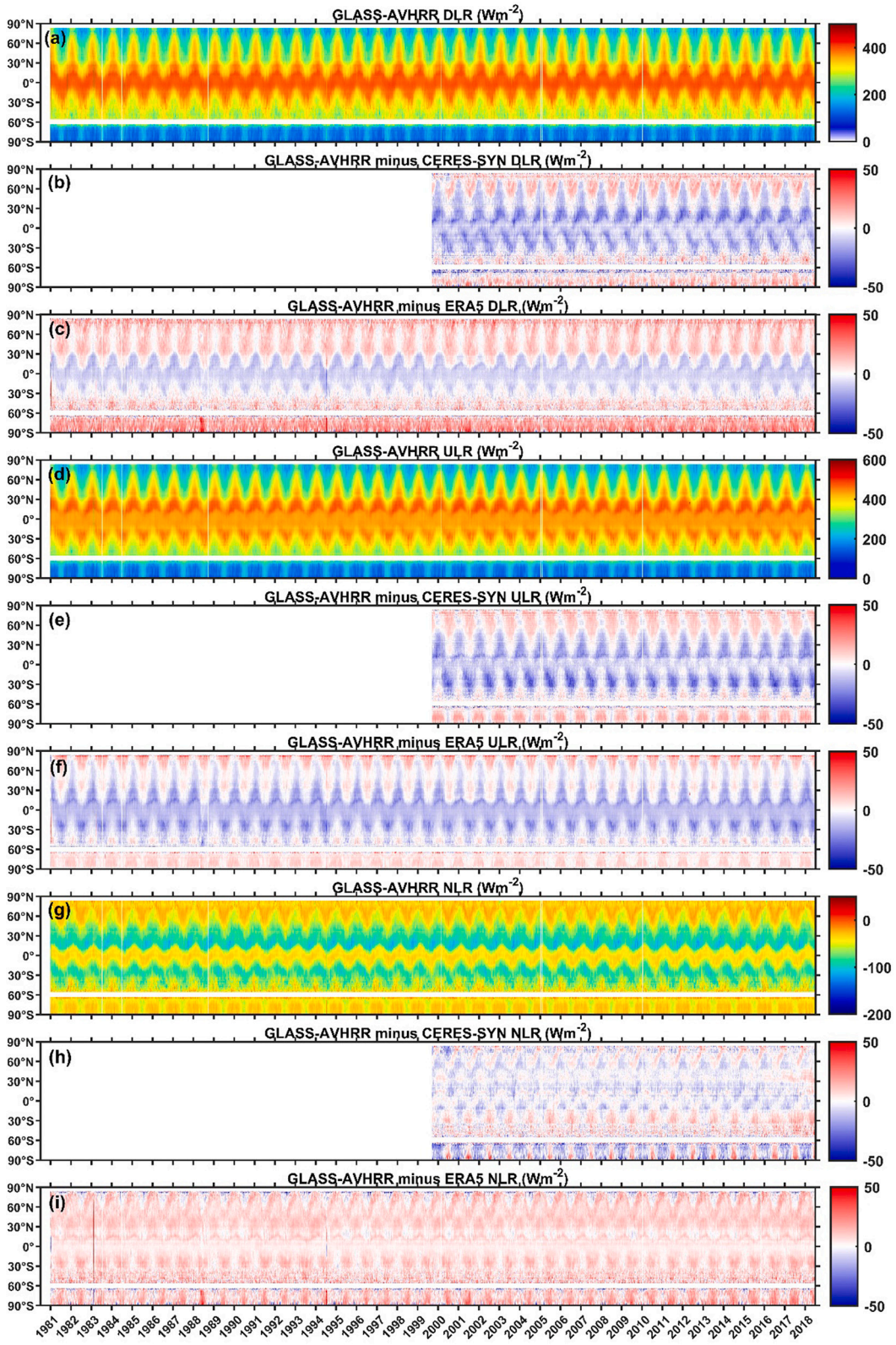

Fig. 10. Temporal variations in the GLASS-AVHRR zonal mean daily global SLWR and their differences against CERES-SYN and ERA5 zonal mean daily global SLWR estimates from 1981 to 2018. Temporal variations for (a–c) DLR, (d–f) ULR, and (g–i) NLR. Positive values (red) indicate GLASS-AVHRR estimates are larger. Blank space represents the lack of values for CERES-SYN before 2000 and over the oceans for the entire period. (For interpretation of the references to colour in this figure legend, the reader is referred to the web version of this article.)

Table 5
Accuracy of GLASS-AVHRR SLWR retrievals for DLR, ULR, NLR using different input features for DesCNN modeling. Inputs-I includes AVHRR TOA BTs for channels 3–5; Inputs-II consists of AVHRR TOA reflectance and BT for channels 1–5; Inputs-III combines CWV, T_a, RH; inputs-IV includes AVHRR TOA BTs for channels 3–5, CWV, T_a, RH, and inputs-V includes AVHRR TOA reflectance and BTs for channels 1–5, CWV, T_a, RH. Units of MEB and RMSE are Wm^{-2}.

Feature group	DLR			ULR			NLR		
	R^2	RMSE	MBE	R^2	RMSE	MBE	R^2	RMSE	MBE
Inputs-I	0.75	33.41	0.46	0.86	26.61	0.30	0.65	20.17	0.07
Inputs-II	0.80	28.74	−1.92	0.89	24.56	−3.18	0.70	18.63	0.91
Inputs-III	0.91	22.63	4.65	0.95	16.90	4.54	0.68	19.00	−0.06
Inputs-IV	0.92	19.96	−2.80	0.96	15.65	−2.98	0.77	16.63	−0.38
Inputs-V	0.92	19.00	−2.57	0.96	15.39	−3.46	0.77	16.10	0.57

AVHRR SLWR retrievals was obtained only when using AVHRR TOA BTs, which revealed the insufficient information regarding TOA BTs with respect to estimating all-sky SLWR (Inputs-I). When AVHRR TOA reflectance was included, the RMSEs of GLASS-AVHRR SLWR retrievals decreased for three longwave components (Inputs-II). Shortwave reflectance decreased the overall uncertainty of all-sky GLASS-AVHRR SLWR by providing information regarding atmospheric and cloud properties. Additionally, when near-surface meteorological variables were individually employed as features (Inputs-III), the uncertainty of GLASS-AVHRR SLWR retrievals decreased significantly. The weighting function of SLWR peaked near the surface (Schmetz, 1989b), illustrating that accurate SLWR values could be retrieved by accessing near-surface meteorological information only. The accuracy of estimated all-sky SLWR was further improved by combing BTs and near-surface meteorological variables (Inputs-IV). This is because the BTs additionally provide meteorological information at higher altitudes, although the atmospheric gases at low-pressure levels contribute little to the ground-level DLR. However, the TOA reflectance seemed to be less important when TOA BTs and near-surface meteorological information has been provided for the DesCNN models (Inputs-V).

To understand whether TOA reflectance can impact the all-sky SLWR estimation, a detailed analysis was further conducted at the site scale. Considering a large improvement in estimated DLR (Inputs-I & -II), the relative differences in RMSEs (δ_{RMSE}) between GLASS-AVHRR DLR retrievals estimated using ($RMSE_{with}$) and without ($RMSE_{without}$) TOA shortwave reflectance were calculated to understand the contribution of shortwave reflectance to DLR estimation, as follows,

$$\delta_{RMSE} = (RMSE_{without} - RMSE_{with})/RMSE_{with} \times 100 \quad (1)$$

Fig. 11(a) shows the spatial distribution of δ_{RMSE} at all sites. Small δ_{RMSE} values occurred at most site locations, resulting in a small difference between Input-IV and -V. However, larger δ_{RMSE} occurred in tropical and polar regions (i.e., Greenland and Antarctica), illustrating the significant contributions of TOA reflectance in these latitudinal zones. Generally, cloud cover in polar regions is higher than that in middle and low latitudes, while CWV in tropical areas is higher than that in other latitudinal zones (Stephens et al., 2012). As the two most important longwave radiation emitters, ERA5-provided CF and CWV were used to understand the contribution of AVHRR TOA shortwave reflectance. When CF > 0.4, the TOA shortwave reflectance contributed to GLASS-AVHRR DLR retrievals in polar regions (δ_{RMSE} of 8% to 16%; Fig. 11b). As the overall CWV is small at the poles, the contribution of TOA shortwave reflectance to GLASS-AVHRR DLR was not significant at the different CWV conditions (Fig. 11c). Additionally, TOA shortwave reflectance had an impact on DLR retrievals at high CF and CWV conditions in tropical regions. As CF increased, δ_{RMSE} increased from 10% to 20%, showing that the contribution of TOA shortwave reflectance was more significant with high CFs (Fig. 11d). When there is high CWV (> 32 $kg.m^{-2}$), similar conclusions can be drawn for tropical areas where shortwave reflectance plays an important role with respect to estimating GLASS-AVHRR DLR values with δ_{RMSE} ranging from 15 to 25%.

Consequently, TOA shortwave reflectance makes a function in DLR estimation in tropical and polar regions. When there is high CF (>0.4) in polar regions, the effect of shortwave reflectance becomes significant and is useful for estimating all-sky DLR. Compared with polar regions, the contribution of shortwave reflectance was more significant in tropical areas with respect to estimating all-sky DLR retrievals, particularly at high CF and CWV conditions. Therefore, TOA shortwave reflectance is a meaningful input feature for DesCNN models with respect to estimating DLR values in polar and particularly tropical areas by providing implicit properties of the atmosphere and clouds. However, considering that the spectral resolution of the AVHRR sensor is coarse, other multispectral sensors (like MODIS) may provide more evidence about the contributions of TOA reflectance at different visible and near-infrared wavebands to the all-sky DLR estimation. Also, we suspect that the contribution of TOA reflectance may depend on the height and type of the cloud, which needs a more explicit analysis in the future study.

6. Discussion

The high accuracy of GLASS-AVHRR SLWR products reflects the advantages of comprehensive input features, the integration of current high-quality SLWR products, the direct estimation algorithm, and the architecture and data-mining ability of the DesCNN models. To definitively show the advantage of integrated SLWR samples, we used the integrated samples from three SLWR products and individual SLWR datasets to train two different DesCNN models and compared the uncertainty changes in GLASS-AVHRR SLWR retrievals (Table 6). The highest accuracy was obtained when all three products were employed to generate the integrated SLWR samples. In contrast, the improvements to GLASS-AVHRR SLWR retrievals were limited as the RMSE only decreased by ~1–2 Wm^{-2} for the three SLWR components, compared to the results obtained using individual dataset integration. Theoretically, multiple product integration is more reasonable because bias from each product can be offset in an averaging sense and the dependency of estimates on individual products is also decreased.

Further, we employed instantaneous AVHRR TOA observations to retrieve daily SLWR values in this study. This seems unreasonable as instantaneous satellite 'snapshots' cannot capture the diurnal variation in SLWR. Theoretically, a two-step algorithm should be adopted to estimate daily SLWR based on polar-orbiting satellite observations, in which instantaneous SLWR values are first estimated at the time of satellite measurements and daily SLWR values are subsequently calculated using the temporal upscaling methods. The GLASS-MODIS daily SLWR products were generated based on the two-step algorithm. The clear-sky hybrid algorithm was first used to estimate instantaneous SLWR values from MODIS data (Cheng et al., 2017; Cheng and Liang, 2016); linear sine interpolation was used to retrieve daily SLWR values subsequently (Zeng and Cheng, 2021). The large uncertainty of GLASS-MODIS SLWR estimates—mainly induced by the cloudy-sky SLWR and sine interpolation method—demonstrates that the two-step algorithm cannot estimate accurate daily SLWR values. The cloudy-sky GLASS-MODIS DLR was calculated using the single-layer cloud model (Forman and Margulis, 2007) that uses cloud top temperature to calculate cloud-emitting longwave radiation. However, the factor needed to control cloud-emitting longwave radiation is cloud base temperature, which has

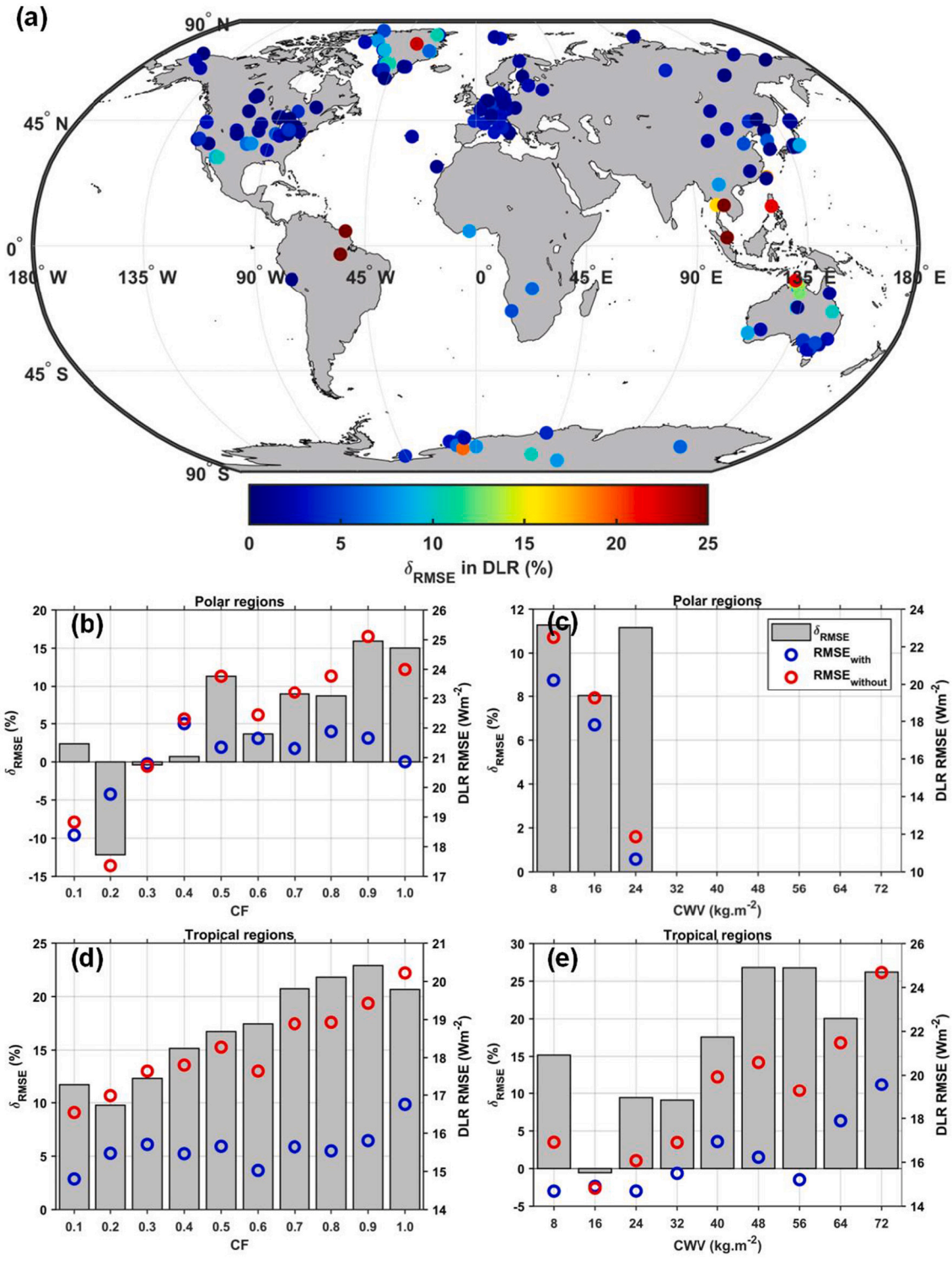

Fig. 11. Contribution of the AVHRR TOA shortwave reflectance to GLASS-AVHRR DLR retrievals. (a) is the spatial distribution of δ_{RMSE}. (b) and (c) are RMSE variations of GLASS-AVHRR DLR values as a function of cloud fraction and CWV in polar regions. (d–e) same as (b–c) but for tropical regions. Red and blue circles denote $RMSE_{without}$ and $RMSE_{with}$, which show the DesCNN DLR RMSEs with and without AVHRR TOA reflectance. Gray bar represents δ_{RMSE}. (For interpretation of the references to colour in this figure legend, the reader is referred to the web version of this article.)

a large temperature difference with respect to the cloud top (Wang et al., 2018). Additionally, the sine interpolation is based on half-sine variation during the daytime and linear variation during the nighttime, which inevitably introduces errors in the final daily SLWR values.

Comparatively, considering the good relationships between instantaneous and daily radiation, it is better to use instantaneous satellite observations to directly estimate daily SLWR values based on the ML methods. The direct estimation algorithm avoids additional errors brought by the temporal upscaling method and has been successfully used in several studies (Chen et al., 2020; Wang et al., 2015; Wang and Liang, 2017). However, to further improve the daily SLWR estimates, diurnal variation information regarding the surface and atmosphere is

Table 6
Accuracy statistics of GLASS-AVHRR SLWR values for DLR, ULR, and NLR when different products were used to generate the integrated samples to train the model. Units of RMSE and MBE are Wm^{-2}. C + E + G represents three products all used in the generation of integrated SLWR samples.

Product	DLR			ULR			NLR		
	R^2	RMSE	MBE	R^2	RMSE	MBE	R^2	RMSE	MBE
CERES-SYN	0.92	21.01	−6.24	0.95	17.61	−6.79	0.76	16.59	0.51
ERA5	0.92	20.09	−3.80	0.95	16.12	−3.67	0.75	16.84	−0.31
GLASS-MODIS	0.92	20.26	2.34	0.96	15.70	2.26	0.74	17.59	0.58
C + E + G	0.92	19.00	−2.57	0.96	15.39	−3.49	0.77	16.10	0.57

still needed. This is solved by incorporating geostationary satellite observations with a finer temporal resolution (e.g., CERES-SYN) and providing additional atmospheric parameters at the daily scale (Xu et al., 2020). Therefore, ERA5 meteorological parameters were employed at a daily time scale to mitigate the influence of temporal scale differences on the GLASS-AVHRR SLWR estimates.

Finally, the success of retrieving GLASS-AVHRR SLWR estimates can be largely attributed to the strong data mining of DesCNN model and its architecture design. The relationship between satellite TOA observations and SLWR is highly complicated and is a comprehensive function of the surface, cloud, and atmospheric properties. Layers in DesCNN can receive feature maps from all preceding layers as inputs to generate diversified features and richer patterns, which facilitate the acquisition of "collective knowledge." These rich features and patterns assist in learning the complicated relationships between satellite signals and in situ SLWR observations, resulting in more accurate SLWR estimates. Due to the channel-wise concatenation throughout its dense blocks, DesCNN maintains both low- and high-level complexity features to handle multi-level features contributes to better SLWR estimates. In addition, DesCNN incorporates the spatially neighboring information about the surface and atmosphere rather than the information at individual pixels approximately to estimate SLWR, which is particularly important in high-resolution satellite images due to the 3-D radiative effects of clouds and the atmosphere (Wyser et al., 2005; Xu et al., 2022).

7. Conclusions

SLWR is a critical component of the Earth's total energy and drives the surface energy balance at the interface between the Earth's surface and atmosphere. Current satellite-derived SLWR products have different limitations, such as a relatively short period (e.g., CERES-SYN), coarse spatial resolution (e.g., GEWEX-SRB, CERES-SYN), and clear-sky instantaneous estimation (e.g., GLASS-MODIS), that hinder their in-depth applications in hydrological, meteorological, agricultural, and climate analysis. A long-term, high-resolution, accurate daily mean SLWR product is still needed for numerical modeling and climate change. In this study, we developed an effective methodology for obtaining a 38-year (1981–2018) daily SLWR dataset at 5 km spatial resolution from AVHRR TOA observations and ERA5 meteorological data using multiple densely connected neural networks (DesCNNs). The DesCNN models were developed using an integrated SLWR sample dataset from CERES-SYN, ERA5, and GLASS-MODIS SLWR retrievals to synergize superior SLWR products. Specifically, the DesCNN models accurately estimated the GLASS-AVHRR SLWR values under the all-sky condition by establishing statistical relationships among the integrated SLWR samples, AVHRR TOA shortwave reflectance, thermal BTs, sun-viewing geometry (SZA, VZA, RAA), and ERA5 near-surface meteorological variables (i.e., T_a, CWV, RH). Transfer learning was used to correct the variation in SLWR when $T_a < 230$ K. We found that AVHRR TOA shortwave reflectance had a significant contribution to the all-sky DLR estimation in tropical and polar regions where high CF or CWV exist.

We evaluated the GLASS-AVHRR SLWR products using independent datasets of in situ observations from globally distributed stations and space-based products, including CERES-SYN, ERA5, and GLASS-MODIS. The all-sky GLASS-AVHRR SLWR dataset had overall RMSEs of 18.66, 14.92, and 16.29 Wm^{-2} and MBEs of −2.69, −3.77, and 0.49 Wm^{-2} for DLR, ULR, and NLR, respectively. Additionally, the GLASS-AVHRR SLWR products had comparable or better accuracies than the CERES-SYN, ERA5, and GLASS-MODIS products under most surface and meteorological conditions (the exceptions being high CWV in tropical areas). The GLASS-AVHRR SLWR products had reasonable spatial distributions and good temporal consistency compared with the CERES-SYN and ERA5 datasets. We believe that these newly archived products will play an important role in climate change studies (e.g., Arctic amplification) owing to their long duration (1981–2018), high spatial resolution (5 km), good internal consistency, and high accuracy.

However, systematic underestimation in GLASS-AVHRR SLWR products occurs in tropical areas. This underestimation is mainly attributable to the local overfitting of DesCNN models at high values, which is induced by the non-uniform SLWR sample distribution across the globe. In future work, we will address this underestimation at high values using methods to increase the sample number (data augmentation, synthetic minority over-sampling) or post-correction of SLWR estimates (cumulative distribution function matching). Additionally, geostationary satellite observations can be incorporated to further improve the accuracy of GLASS-AVHRR SLWR retrievals by providing diurnal variation information regarding the surface and atmosphere. Finally, an ensemble learning scheme will be adopted to obtain more accurate SLWR values by taking full advantage of different neural network architectures.

Credit author statement

Jianglei Xu: Data curation, Formal analysis, Investigation, Methodology, Resources, Software, Validation, Visualization, Writing - original draft, Writing - review & editing. Shunlin Liang: Conceptualization, Funding acquisition, Project administration, Supervision, Writing review & editing. Han Ma and Tao He: Writing - review & editing.

Declaration of Competing Interest

The authors declare that they have no known competing financial interests or personal relationships that could have appeared to influence the work reported in this paper.

Data availability

Data will be made available at www.glass.umd.edu and www.geodata.cn.

Acknowledgments

This study was supported by the Chinese Grand Research Program on Climate Change and Response project [2016YFA0600103]. The authors would like to thank the LTDR project for providing the AVH02C1 product, the CERES team for offering the CERES-SYN product, the ECMWF project for the ERA5 product and the GLASS team for the GLASS-MODIS SLWR product. We thank various networks/programs for offering in situ measurements. We also acknowledge data support from

the "National Earth System Science Data Center, National Science & Technology Infrastructure of China (http://www.geodata.cn)".

Appendix A. Supplementary data

Supplementary data to this article can be found online at https://doi.org/10.1016/j.rse.2022.113223.

References

Augustine, J.A., DeLuisi, J.J., Long, C.N., 2000. SURFRAD–A national surface radiation budget network for atmospheric research. Bull. Am. Meteorol. Soc. 81, 2341–2358.

Baret, F., Weiss, M., Lacaze, R., Camacho, F., Makhmara, H., Pacholcyzk, P., Smets, B., 2013. GEOV1: LAI and FAPAR essential climate variables and FCOVER global time series capitalizing over existing products. Part1: principles of development and production. Remote Sens. Environ. 137, 299–309. https://doi.org/10.1016/j.rse.2012.12.027.

Bilgiç, H.H., Mert, İ., 2021. Comparison of different techniques for estimation of incoming longwave radiation. Int. J. Environ. Sci. Technol. 18, 601–618.

Carmona, F., Rivas, R., Caselles, V., 2014. Estimation of daytime downward longwave radiation under clear and cloudy skies conditions over a sub-humid region. Theor. Appl. Climatol. 115, 281–295. https://doi.org/10.1007/s00704-013-0891-3.

Casey, K.S., Brandon, T.B., Cornillon, P., Evans, R., 2010. The past, present, and future of the AVHRR Pathfinder SST program. In: Oceanography from Space, 273-287. Springer.

Chen, X., Long, D., Liang, S., He, L., Zeng, C., Hao, X., Hong, Y., 2018. Developing a composite daily snow cover extent record over the Tibetan Plateau from 1981 to 2016 using multisource data. Remote Sens. Environ. 215, 284–299. https://doi.org/10.1016/j.rse.2018.06.021.

Chen, J., He, T., Jiang, B., Liang, S., 2020. Estimation of all-sky all-wave daily net radiation at high latitudes from MODIS data. Remote Sens. Environ. 245, 111842.

Cheng, J., Liang, S., 2016. Global estimates for high-spatial-resolution clear-sky land surface upwelling longwave radiation from MODIS data. IEEE Trans. Geosci. Remote Sens. 54, 4115–4129.

Cheng, J., Liang, S., Verhoef, W., Shi, L., Liu, Q., 2015. Estimating the hemispherical broadband longwave emissivity of global vegetated surfaces using a radiative transfer model. IEEE Trans. Geosci. Remote Sens. 54, 905–917.

Cheng, J., Liang, S., Wang, W., Guo, Y., 2017. An efficient hybrid method for estimating clear-sky surface downward longwave radiation from MODIS data. J. Geophys. Res.-Atmos. 122, 2616–2630. https://doi.org/10.1002/2016JD026250.

Cheng, J., Yang, F., Guo, Y., 2019. A comparative study of bulk parameterization schemes for estimating cloudy-sky surface downward longwave radiation. Remote Sens. 11, 528.

Chollet, F., 2017. Xception: Deep learning with depthwise separable convolutions. In: Proceedings of the IEEE Conference on Computer Vision and Pattern Recognition, pp. 1251–1258.

Crawford, T.M., Duchon, C.E., 1999. An improved parameterization for estimating effective atmospheric emissivity for use in calculating daytime downwelling longwave radiation. J. Appl. Meteorol. 38, 474–480.

Dewitte, S., Clerbaux, N., 2018. Decadal Changes of Earth's Outgoing Longwave Radiation.

Doelling, D.R., Loeb, N.G., Keyes, D.F., Nordeen, M.L., Morstad, D., Nguyen, C., Wielicki, B.A., Young, D.F., Sun, M., 2013. Geostationary enhanced temporal interpolation for CERES flux products. J. Atmos. Ocean. Technol. 30, 1072–1090.

Doelling, D.R., Sun, M., Nguyen, L.T., Nordeen, M.L., Haney, C.O., Keyes, D.F., Mlynczak, P.E., 2016. Advances in geostationary-derived longwave fluxes for the CERES synoptic (SYN1deg) product. J. Atmos. Ocean. Technol. 33, 503–521.

dos Santos Nascimento, G., Ruhoff, A., Cavalcanti, J.R., da Motta Marques, D., Roberti, D.R., da Rocha, H.R., Munar, A.M., Fragoso, C.R., de Oliveira, M.B.L., 2019. Assessing CERES surface radiation components for tropical and subtropical biomes. IEEE J. Sel. Top. Appl. Earth Obs. Remote Sens. 12, 3826–3840.

Eastman, R., Warren, S.G., 2013. A 39-yr survey of cloud changes from land stations worldwide 1971–2009: Long-term trends, relation to aerosols, and expansion of the tropical belt. J. Clim. 26, 1286–1303.

Ellingson, R.G., 1995. Surface longwave fluxes from satellite observations: a critical review. Remote Sens. Environ. 51, 89–97.

Evans, R., Casey, K., Cornillon, P., 2010. Transition of AVHRR SST Pathfinder to Version 6, Continued Evolution of a CDR.

Fausto, R.S., van As, D., Mankoff, K.D., Vandecrux, B., Citterio, M., Ahlstrøm, A.P., Andersen, S.B., Colgan, W., Karlsson, N.B., Kjeldsen, K.K., 2021. Programme for Monitoring of the Greenland Ice Sheet (PROMICE) automatic weather station data. Earth Syst. Sci. Data 13, 3819–3845.

Feng, C., Zhang, X., Wei, Y., Zhang, W., Hou, N., Xu, J., Jia, K., Yao, Y., Xie, X., Jiang, B., 2020. Estimating surface downward longwave radiation using machine learning methods. Atmosphere 11, 1147.

Forman, B.A., Margulis, S.A., 2007. Estimates of total downwelling surface radiation using a high-resolution GOES-based cloud product along with MODIS and AIRS products. In: AGU Fall Meeting Abstracts, H31A-0134.

Franch, B., Vermote, E.F., Roger, J.-C., Murphy, E., Becker-Reshef, I., Justice, C., Claverie, M., Nagol, J., Csiszar, I., Meyer, D., Baret, F., Masuoka, E., Wolfe, R., Devadiga, S., 2017. A 30+ year AVHRR land surface reflectance climate data record and its application to wheat yield monitoring. Remote Sens. 9, 296.

Frederick, J.E., Tinsley, B.A., 2018. The response of longwave radiation at the South Pole to electrical and magnetic variations: links to meteorological generators and the solar wind. J. Atmos. Sol. Terr. Phys. 179, 214–224.

Fu, Q., Liou, K., 1992. On the correlated k-distribution method for radiative transfer in nonhomogeneous atmospheres. J. Atmos. Sci. 49, 2139–2156.

Gao, X., Liang, S., Sauer, J., 2020. Greening hiatus in Eurasian boreal forests since 1997 caused by a wetting and cooling summer climate. J. Geophys. Res. Biogeosci. 125 e2020JG005662.

Gharekhan, D., Bhattacharya, B.K., Desai, D., Patel, P.R., 2021. Neural network-based approach for estimation of downwelling longwave radiation flux under cloudy-sky conditions. J. Appl. Remote. Sens. 15, 024515.

Goosse, H., Kay, J.E., Armour, K.C., Bodas-Salcedo, A., Chepfer, H., Docquier, D., Jonko, A., Kushner, P.J., Lecomte, O., Massonnet, F., 2018. Quantifying climate feedbacks in polar regions. Nat. Commun. 9, 1–13.

Gui, S., Liang, S., Li, L., 2010. Evaluation of satellite-estimated surface longwave radiation using ground-based observations. J. Geophys. Res.-Atmos. 115.

Guo, Y., Cheng, J., Liang, S., 2019. Comprehensive assessment of parameterization methods for estimating clear-sky surface downward longwave radiation. Theor. Appl. Climatol. 135, 1045–1058. https://doi.org/10.1007/s00704-018-2423-7.

Guo, W., Du, H., Guo, C., Southwell, B.J., Cheong, J.W., Dempster, A.G., 2022. Information fusion for GNSS-R wind speed retrieval using statistically modified convolutional neural network. Remote Sens. Environ. 272, 112934 https://doi.org/10.1016/j.rse.2022.112934.

Gupta, S.K., Kratz, D.P., Wilber, A.C., Nguyen, L.C., 2004. Validation of parameterized algorithms used to derive TRMM–CERES surface radiative fluxes. J. Atmos. Ocean. Technol. 21, 742–752.

Gupta, S., Stackhouse, P., Cox, S., Mikovitz, C., Zhang, T., 2008. The NASA/GEWEX Surface Radiation Budget Dataset, 37th COSPAR Scientific Assembly, 37, p. 1125.

Hao, D., Asrar, G., Zeng, Y., Zhu, Q., Wen, J., Xiao, Q., Chen, M., 2019. Estimating hourly land surface downward shortwave and photosynthetically active radiation from DSCOVR/EPIC observations. Remote Sens. Environ. 232, 111320.

He, T., Liang, S., Wang, D., Shuai, Y., Yu, Y., 2013. Fusion of satellite land surface albedo products across scales using a multiresolution tree method in the north Central United States. IEEE Trans. Geosci. Remote Sens. 52, 3428–3439.

He, K., Zhang, X., Ren, S., Sun, J., 2016. Deep Residual Learning for Image Recognition, 2016 IEEE Conference on Computer Vision and Pattern Recognition (CVPR), pp. 770–778. https://doi.org/10.1109/CVPR.2016.90.

Hersbach, H., Bell, B., Berrisford, P., Hirahara, S., Horányi, A., Muñoz-Sabater, J., Nicolas, J., Peubey, C., Radu, R., Schepers, D., 2020. The ERA5 global reanalysis. Q. J. R. Meteorol. Soc. 146, 1999–2049.

Huang, G., Liu, Z., Van Der Maaten, L., Weinberger, K.Q., 2017. Densely connected convolutional networks. In: Proceedings of the IEEE Conference on Computer Vision and Pattern Recognition, pp. 4700–4708.

Huang, X., Zhu, D., Zhang, F., Liu, T., Li, X., Zou, L., 2021. Sensing population distribution from satellite imagery via deep learning:model selection, neighboring effects, and systematic biases. IEEE J. Sel. Top. Appl. Earth Obs. Remote Sens. 14, 5137–5151. https://doi.org/10.1109/JSTARS.2021.3076630.

Iandola, F., Moskewicz, M., Karayev, S., Girshick, R., Darrell, T., Keutzer, K., 2014. Densenet: Implementing Efficient Convnet Descriptor Pyramids. arXiv preprint arXiv:1404.1869.

Jia, A., Liang, S., Jiang, B., Zhang, X., Wang, G., 2018. Comprehensive assessment of global surface net radiation products and uncertainty analysis. J. Geophys. Res.-Atmos. 123, 1970–1989.

Jia, K., Yang, L., Liang, S., Xiao, Z., Zhao, X., Yao, Y., Zhang, X., Jiang, B., Liu, D., 2019. Long-term global land surface satellite (GLASS) fractional vegetation cover product derived from MODIS and AVHRR data. IEEE J. Sel. Top. Appl. Earth Obs. Remote Sens. 12, 508–518. https://doi.org/10.1109/JSTARS.2018.2854293.

Jia, A., Liang, S., Wang, D., Jiang, B., Zhang, X., 2020. Air pollution slows down surface warming over the Tibetan Plateau. Atmos. Chem. Phys. 20, 881–899.

Jiang, B., Liang, S., Jia, A., Xu, J., Zhang, X., Xiao, Z., Zhao, X., Jia, K., Yao, Y., 2018. Validation of the surface daytime net radiation product from version 4.0 GLASS product suite. IEEE Geosci. Remote Sens. Lett. 16, 509–513.

Jiao, Z.-H., Mu, X., 2022. Global validation of clear-sky models for retrieving land-surface downward longwave radiation from MODIS data. Remote Sens. Environ. 271, 112903 https://doi.org/10.1016/j.rse.2022.112903.

Karlsson, K.G., Riihelä, A., Müller, R., Meirink, J.F., Sedlar, J., Stengel, M., Lockhoff, M., Trentmann, J., Kaspar, F., Hollmann, R., Wolters, E., 2013. CLARA-A1: a cloud, albedo, and radiation dataset from 28 yr of global AVHRR data. Atmos. Chem. Phys. 13, 5351–5367. https://doi.org/10.5194/acp-13-5351-2013.

Karlsson, K.G., Anttila, K., Trentmann, J., Stengel, M., Fokke Meirink, J., Devasthale, A., Hanschmann, T., Kothe, S., Jääskeläinen, E., Sedlar, J., Benas, N., van Zadelhoff, G. J., Schlundt, C., Stein, D., Finkensieper, S., Håkansson, N., Hollmann, R., 2017. CLARA-A2: the second edition of the CM SAF cloud and radiation data record from 34 years of global AVHRR data. Atmos. Chem. Phys. 17, 5809–5828. https://doi.org/10.5194/acp-17-5809-2017.

King, M.D., Platnick, S., Menzel, W.P., Ackerman, S.A., Hubanks, P.A., 2013. Spatial and temporal distribution of clouds observed by MODIS onboard the Terra and Aqua satellites. IEEE Trans. Geosci. Remote Sens. 51, 3826–3852.

Kofroňová, J., Tesař, M., Šípek, V., 2019. The influence of observed and modelled net longwave radiation on the rate of estimated potential evapotranspiration. J. Hydrol. Hydromech. 67, 280–288.

Koll, D.D., Cronin, T.W., 2018. Earth's outgoing longwave radiation linear due to H2O greenhouse effect. Proc. Natl. Acad. Sci. 115, 10293–10298.

Kuipers Munneke, P., Van den Broeke, M., King, J., Gray, T., Reijmer, C., 2012. Near-surface climate and surface energy budget of Larsen C ice shelf, Antarctic Peninsula. Cryosphere 6, 353–363.

LeCun, Y., Bengio, Y., Hinton, G., 2015. Deep learning. Nature 521, 436–444.
Letu, H., Nakajima, T.Y., Wang, T., Shang, H., Ma, R., Yang, K., Baran, A.J., Riedi, J., Ishimoto, H., Yoshida, M., 2021. A new benchmark for surface radiation products over the East Asia-Pacific region retrieved from the Himawari-8/AHI next-generation geostationary satellite. Bull. Am. Meteorol. Soc. 1-40.
Li, R., Wang, D., Liang, S., Jia, A., Wang, Z., 2022. Estimating global downward shortwave radiation from VIIRS data using a transfer-learning neural network. Remote Sens. Environ. 274, 112999 https://doi.org/10.1016/j.rse.2022.112999.
Liang, S., Wang, K., Zhang, X., Wild, M., 2010. Review on estimation of land surface radiation and energy budgets from ground measurement, remote sensing and model simulations. IEEE J. Sel. Top. Appl. Earth Obs. Remote Sens. 3, 225–240.
Liang, S., Wang, D., Tao, X., Cheng, J., Yao, Y., Zhang, X., He, T., 2018. Methodologies for Integrating Multiple High-Level Remotely Sensed Land Products.
Liang, S., Wang, D., He, T., Yu, Y., 2019. Remote sensing of earth's energy budget: synthesis and review. Int. J. Digital Earth 12, 737–780.
Liang, S., Cheng, J., Jia, K., Jiang, B., Liu, Q., Xiao, Z., Yao, Y., Yuan, W., Zhang, X., Zhao, X., 2021a. The global LAnd surface satellite (GLASS) product suite. Bull. Am. Meteorol. Soc. 1-37.
Liang, S., Cheng, J., Jia, K., Jiang, B., Liu, Q., Xiao, Z., Yao, Y., Yuan, W., Zhang, X., Zhao, X., 2021b. The global land surface satellite (GLASS) product suite. Bull. Am. Meteorol. Soc. 102, E323–E337.
Lindsay, R., Wensnahan, M., Schweiger, A., Zhang, J., 2014. Evaluation of seven different atmospheric reanalysis products in the Arctic. J. Clim. 27, 2588–2606.
Liu, M., Zheng, X., Zhang, J., Xia, X., 2020. A revisiting of the parametrization of downward longwave radiation in summer over the Tibetan Plateau based on high-temporal-resolution measurements. Atmos. Chem. Phys. 20, 4415–4426. https://doi.org/10.5194/acp-20-4415-2020.
Liu, Z., Lang, X., Jiang, D., 2021. Impact of stratospheric aerosol intervention geoengineering on surface air temperature in China: a surface energy budget perspective. Atmos. Chem. Phys. Discuss. 1-29, 2021. https://doi.org/10.5194/acp-2021-503.
Loeb, N.G., Manalo-Smith, N., Kato, S., Miller, W.F., Gupta, S.K., Minnis, P., Wielicki, B. A., 2003. Angular distribution models for top-of-atmosphere radiative flux estimation from the clouds and the earth's radiant energy system instrument on the tropical rainfall measuring mission satellite. Part I: methodology. J. Appl. Meteorol. 42, 240–265.
Lopes, F.M., Dutra, E., Trigo, I.F., 2022. Integrating reanalysis and satellite cloud information to estimate surface downward long-wave radiation. Remote Sens. 14, 1704.
Ma, J., Zhou, J., Göttsche, F.M., Liang, S., Wang, S., Li, M., 2020. A global long-term (1981-2000) land surface temperature product for NOAA AVHRR. Earth Syst. Sci. Data Discuss. 1-43, 2020. https://doi.org/10.5194/essd-2020-143.
Naud, C.M., Chen, Y., Rangwala, I., Miller, J.R., 2013. Sensitivity of downward longwave surface radiation to moisture and cloud changes in a high-elevation region. J. Geophys. Res.-Atmos. 118 https://doi.org/10.1002/jgrd.50644, 10,072-010,081.
Newman, M., Sardeshmukh, P.D., Bergman, J.W., 2000. An assessment of the NCEP, NASA, and ECMWF reanalyses over the tropical West Pacific warm pool. Bull. Am. Meteorol. Soc. 81, 41–48.
Niemelä, S., Räisänen, P., Savijärvi, H., 2001. Comparison of surface radiative flux parameterizations: part I: longwave radiation. Atmos. Res. 58, 1–18.
Ohmura, A., Dutton, E.G., Forgan, B., Fröhlich, C., Gilgen, H., Hegner, H., Heimo, A., König-Langlo, G., McArthur, B., Müller, G., 1998. Baseline surface radiation network (BSRN/WCRP): new precision radiometry for climate research. Bull. Am. Meteorol. Soc. 79, 2115–2136.
Pedelty, J., Devadiga, S., Masuoka, E., Brown, M., Pinzon, J., Tucker, C., Vermote, E., Prince, S., Nagol, J., Justice, C., Roy, D., Junchang, J., Schaaf, C., Jicheng, L., Privette, J., Pinheiro, A., 2007. Generating a Long-term Land Data Record from the AVHRR and MODIS Instruments, 2007 IEEE International Geoscience and Remote Sensing Symposium, 23–28 July 2007, pp. 1021–1025. https://doi.org/10.1109/IGARSS.2007.4422974.
Qin, B., Cao, B., Bian, Z., Li, R., Li, H., Ran, X., Du, Y., Xiao, Q., Liu, Q., 2021. Clear-sky land surface upward longwave radiation dataset derived from the ABI onboard the GOES–16 satellite. Big Earth Data 1-21.
Refaeilzadeh, P., Tang, L., Liu, H., 2009. Cross-validation. In: Encyclopedia of Database Systems, 5, pp. 532–538.
Ruckstuhl, C., Philipona, R., Morland, J., Ohmura, A., 2007. Observed relationship between surface specific humidity, integrated water vapor, and longwave downward radiation at different altitudes. J. Geophys. Res.-Atmos. 112.
Rutan, D.A., Kato, S., Doelling, D.R., Rose, F.G., Nguyen, L.T., Caldwell, T.E., Loeb, N.G., 2015a. CERES synoptic product: methodology and validation of surface radiant flux. J. Atmos. Ocean. Technol. 32, 1121–1143.
Rutan, D.A., Kato, S., Doelling, D.R., Rose, F.G., Nguyen, L.T., Caldwell, T.E., Loeb, N.G., 2015b. CERES synoptic product: methodology and validation of surface radiant flux. J. Atmos. Ocean. Technol. 32, 1121–1143.
Schmetz, J., 1989a. Towards a surface radiation climatology: retrieval of downward irradiances from satellites. Atmos. Res. 23, 287–321.
Schmetz, J., 1989b. Towards a surface radiation climatology: retrieval of downward irradiances from satellites. Atmos. Res. 23, 287–321. https://doi.org/10.1016/0169-8095(89)90023-9.
Sengupta, A., Ye, Y., Wang, R., Liu, C., Roy, K., 2019. Going deeper in spiking neural networks: VGG and residual architectures. Front. Neurosci. 13, 95.
Shang, K., Yao, Y., Liang, S., Zhang, Y., Fisher, J.B., Chen, J., Liu, S., Xu, Z., Zhang, Y., Jia, K., 2021. DNN-MET: a deep neural networks method to integrate satellite-derived evapotranspiration products, eddy covariance observations and ancillary information. Agric. For. Meteorol. 308, 108582.
Shi, G.-Y., Hayasaka, T., Ohmura, A., Chen, Z.-H., Wang, B., Zhao, J.-Q., Che, H.-Z., Xu, L., 2008. Data quality assessment and the long-term trend of ground solar radiation in China. J. Appl. Meteorol. Climatol. 47, 1006–1016.
Shrestha, A., Mahmood, A., 2019. Review of deep learning algorithms and architectures. IEEE Access 7, 53040–53065. https://doi.org/10.1109/ACCESS.2019.2912200.
Stackhouse Jr., P., Gupta, S., Cox, S., Chiacchio, M., Mikovitz, J., 2000. The WCRP/GEWEX Surface Radiation Budget Project Release 2: An Assessment of Surface Fluxes at 1 Degree Resolution.
Stengel, M., Stapelberg, S., Sus, O., Finkensieper, S., Würzler, B., Philipp, D., Hollmann, R., Poulsen, C., Christensen, M., McGarragh, G., 2020. Cloud_cci advanced very high resolution radiometer post meridiem (AVHRR-PM) dataset version 3: 35-year climatology of global cloud and radiation properties. Earth Syst. Sci. Data 12, 41–60.
Stephens, G.L., Wild, M., Stackhouse Jr., P.W., L'Ecuyer, T., Kato, S., Henderson, D.S., 2012. The global character of the flux of downward longwave radiation. J. Clim. 25, 2329–2340.
Szegedy, C., Vanhoucke, V., Ioffe, S., Shlens, J., Wojna, Z., 2016. Rethinking the inception architecture for computer vision. In: Proceedings of the IEEE Conference on Computer Vision and Pattern Recognition, pp. 2818–2826.
Tang, B., Li, Z.-L., 2008. Estimation of instantaneous net surface longwave radiation from MODIS cloud-free data. Remote Sens. Environ. 112, 3482–3492.
Tang, W., Yang, K., He, J., Qin, J., 2010. Quality control and estimation of global solar radiation in China. Sol. Energy 84, 466–475. https://doi.org/10.1016/j.solener.2010.01.006.
Tang, W., Qin, J., Yang, K., Zhu, F., Zhou, X., 2021. Does ERA5 outperform satellite products in estimating atmospheric downward longwave radiation at the surface? Atmos. Res. 252, 105453 https://doi.org/10.1016/j.atmosres.2021.105453.
Trigo, I.F., Barroso, C., Viterbo, P., Freitas, S.C., Monteiro, I.T., 2010. Estimation of downward long-wave radiation at the surface combining remotely sensed data and NWP data. J. Geophys. Res.-Atmos. 115.
Urraca, R., Gracia-Amillo, A.M., Koubli, E., Huld, T., Trentmann, J., Riihelä, A., Lindfors, A.V., Palmer, D., Gottschalg, R., Antonanzas-Torres, F., 2017. Extensive validation of CM SAF surface radiation products over Europe. Remote Sens. Environ. 199, 171–186. https://doi.org/10.1016/j.rse.2017.07.013.
van As, D., Fausto, R.S., Ahlstrøm, A.P., Andersen, S.B., Andersen, M.L., Citterio, M., Edelvang, K., Gravesen, P., Machguth, H., Nick, F.M., 2011. Programme for Monitoring of the Greenland Ice Sheet (PROMICE): first temperature and ablation records. Geol. Surv. Denmark Greenland Bull. 23, 73–76.
Van Den Broeke, M., Reijmer, C., Van De Wal, R., 2004. Surface radiation balance in Antarctica as measured with automatic weather stations. J. Geophys. Res.-Atmos. 109.
Vermote, E., Saleous, N., 2006. Calibration of NOAA16 AVHRR over a desert site using MODIS data. Remote Sens. Environ. 105, 214–220.
Viúdez-Mora, A., Calbó, J., González, J., Jiménez, M., 2009. Modeling atmospheric longwave radiation at the surface under cloudless skies. J. Geophys. Res.-Atmos. 114.
Wang, K., Dickinson, R.E., 2013. Global atmospheric downward longwave radiation at the surface from ground-based observations, satellite retrievals, and reanalyses. Rev. Geophys. 51, 150–185.
Wang, W., Liang, S., 2009. Estimation of high-spatial resolution clear-sky longwave downward and net radiation over land surfaces from MODIS data. Remote Sens. Environ. 113, 745–754. https://doi.org/10.1016/j.rse.2008.12.004.
Wang, W., Liang, S., 2010. A method for estimating clear-sky instantaneous land-surface longwave radiation with GOES sounder and GOES-R ABI data. IEEE Geosci. Remote Sens. Lett. 7, 708–712. https://doi.org/10.1109/LGRS.2010.2046472.
Wang, D., Liang, S., 2017. Estimating top-of-atmosphere daily reflected shortwave radiation flux over land from MODIS data. IEEE Trans. Geosci. Remote Sens. 55, 4022–4031.
Wang, W., Liang, S., Augustine, J.A., 2009. Estimating high spatial resolution clear-sky land surface upwelling longwave radiation from MODIS data. IEEE Trans. Geosci. Remote Sens. 47, 1559–1570. https://doi.org/10.1109/TGRS.2008.2005206.
Wang, T., Yan, G., Chen, L., 2012. Consistent retrieval methods to estimate land surface shortwave and longwave radiative flux components under clear-sky conditions. Remote Sens. Environ. 124, 61–71.
Wang, D., Liang, S., He, T., Shi, Q., 2015. Estimation of daily surface shortwave net radiation from the combined MODIS data. IEEE Trans. Geosci. Remote Sens. 53, 5519–5529.
Wang, C., Tang, B.-H., Huo, X., Li, Z.-L., 2017. New method to estimate surface upwelling long-wave radiation from MODIS cloud-free data. Opt. Express 25, A574–A588. https://doi.org/10.1364/OE.25.00A574.
Wang, T., Shi, J., Yu, Y., Husi, L., Gao, B., Zhou, W., Ji, D., Zhao, T., Xiong, C., Chen, L., 2018. Cloudy-sky land surface longwave downward radiation (LWDR) estimation by integrating MODIS and AIRS/AMSU measurements. Remote Sens. Environ. 205, 100–111. https://doi.org/10.1016/j.rse.2017.11.011.
Wang, D., Liang, S., Li, R., Jia, A., 2021a. A synergic study on estimating surface downward shortwave radiation from satellite data. Remote Sens. Environ. 264, 112639 https://doi.org/10.1016/j.rse.2021.112639.
Wang, G., Wang, T., Xue, H., 2021b. Validation and comparison of surface shortwave and longwave radiation products over the three poles. Int. J. Appl. Earth Obs. Geoinf. 104, 102538.
Wei, Y., Zhang, X., Li, W., Hou, N., Zhang, W., Xu, J., Feng, C., Jia, K., Yao, Y., Cheng, J., 2021. Trends and variability of atmospheric downward longwave radiation over China from 1958 to 2015. Earth Space Sci. 8 e2020EA001370.
Wei, Y., Zhang, X., Wenhong, L., Hou, N., Zhang, W., Jiawen, X., Feng, C., Jia, K., Yao, Y., Cheng, J., 2021. Trends and variability of atmospheric downward longwave

radiation over China from 1958 to 2015. Earth Space Sci. 8 (2) https://doi.org/10.1029/2020EA001370 e2020EA001370.
Wielicki, B.A., Barkstrom, B.R., Baum, B.A., Charlock, T.P., Green, R.N., Kratz, D.P., Lee, R.B., Minnis, P., Smith, G.L., Wong, T., 1998. Clouds and the earth's radiant energy system (CERES): algorithm overview. IEEE Trans. Geosci. Remote Sens. 36, 1127–1141.
Wild, M., Ohmura, A., Gilgen, H., Morcrette, J.-J., Slingo, A., 2001. Evaluation of downward longwave radiation in general circulation models. J. Clim. 14, 3227–3239.
Wilson, K., Goldstein, A., Falge, E., Aubinet, M., Baldocchi, D., Berbigier, P., Bernhofer, C., Ceulemans, R., Dolman, H., Field, C., 2002. Energy balance closure at FLUXNET sites. Agric. For. Meteorol. 113, 223–243.
Wyser, K., O'Hirok, W., Gautier, C., 2005. A simple method for removing 3-D radiative effects in satellite retrievals of surface irradiance. Remote Sens. Environ. 94, 335–342. https://doi.org/10.1016/j.rse.2004.10.003.
Xiao, Z., Liang, S., Wang, J., Chen, P., Yin, X., Zhang, L., Song, J., 2014. Use of general regression neural networks for generating the GLASS leaf area index product from time-series MODIS surface reflectance. IEEE Trans. Geosci. Remote Sens. 52, 209–223. https://doi.org/10.1109/TGRS.2013.2237780.
Xu, J., Jiang, B., Liang, S., Li, X., Wang, Y., Peng, J., Chen, H., Liang, H., Li, S., 2020. Generating a high-resolution time-series ocean surface net radiation product by downscaling J-OFURO3. IEEE Trans. Geosci. Remote Sens. 59, 2794–2809. https://doi.org/10.1109/TGRS.2020.3021585.
Xu, J., Liang, S., Jiang, B., 2022. A global long-term (1981–2019) daily land surface radiation budget product from AVHRR satellite data using a residual convolutional neural network. Earth Syst. Sci. Data 14, 2315–2341. https://doi.org/10.5194/essd-14-2315-2022.
Yamamoto, S., Saigusa, N., Gamo, M., Fujinuma, Y., Inoue, G., Hirano, T., 2005. Findings through the AsiaFlux network and a view toward the future. J. Geogr. Sci. 15, 142–148.
Yang, F., Cheng, J., 2020. A framework for estimating cloudy sky surface downward longwave radiation from the derived active and passive cloud property parameters. Remote Sens. Environ. 248, 111972.
Yang, K., He, J., Tang, W., Qin, J., Cheng, C.C., 2010. On downward shortwave and longwave radiations over high altitude regions: observation and modeling in the Tibetan Plateau. Agric. For. Meteorol. 150, 38–46.
Yeo, H., Park, S.-J., Kim, B.-M., Shiobara, M., Kim, S.-W., Kwon, H., Kim, J.-H., Jeong, J.-H., Park, S.S., Choi, T., 2018. The observed relationship of cloud to surface longwave radiation and air temperature at Ny-Ålesund. Svalbard Tellus B Chem. Phys. Meteorol. 70, 1–10.
Yu, R., Li, S., Zhang, B., Zhang, H., Peng, D., Gao, J., 2021. A deep transfer learning method for estimating fractional vegetation cover of Sentinel-2 multispectral images. IEEE Geosci. Remote Sens. Lett. 19, 1–5.
Yuan, Q., Shen, H., Li, T., Li, Z., Li, S., Jiang, Y., Xu, H., Tan, W., Yang, Q., Wang, J., 2020. Deep learning in environmental remote sensing: achievements and challenges. Remote Sens. Environ. 241, 111716.
Zeng, Q., Cheng, J., 2021. Estimating high-spatial resolution surface daily longwave radiation from the instantaneous global LAnd surface satellite (GLASS) longwave radiation product. Int. J. Digital Earth 1-31.
Zeng, Q., Cheng, J., Dong, L., 2020. Assessment of the long-term high-spatial-resolution global LAnd surface satellite (GLASS) surface longwave radiation product using ground measurements. IEEE J. Sel. Top. Appl. Earth Obs. Remote Sens. 13, 2032–2055. https://doi.org/10.1109/JSTARS.2020.2992472.
Zhang, Y., Rossow, W.B., Lacis, A.A., Oinas, V., Mishchenko, M.I., 2004. Calculation of radiative fluxes from the surface to top of atmosphere based on ISCCP and other global data sets: refinements of the radiative transfer model and the input data. J. Geophys. Res.-Atmos. 109.
Zhang, X., Sorteberg, A., Zhang, J., Gerdes, R., Comiso, J.C., 2008. Recent radical shifts of atmospheric circulations and rapid changes in Arctic climate system. Geophys. Res. Lett. 35.
Zhang, X., Liang, S., Wild, M., Jiang, B., 2015. Analysis of surface incident shortwave radiation from four satellite products. Remote Sens. Environ. 165, 186–202.
Zhou, Y., Kratz, D.P., Wilber, A.C., Gupta, S.K., Cess, R.D., 2007. An improved algorithm for retrieving surface downwelling longwave radiation from satellite measurements. J. Geophys. Res.-Atmos. 112.
Zhou, W., Shi, J., Wang, T., Peng, B., Husi, L., Yu, Y., Zhao, R., 2019. New methods for deriving clear-sky surface longwave downward radiation based on remotely sensed data and ground measurements. Earth Space Sci. 6, 2071–2086.
Zhu, M., Yao, T., Yang, W., Xu, B., Wang, X., 2017. Evaluation of parameterizations of incoming longwave radiation in the high-mountain region of the Tibetan plateau. J. Appl. Meteorol. Climatol. 56, 833–848.
Zhu, F., Li, X., Qin, J., Yang, K., Cuo, L., Tang, W., Shen, C., 2021. Integration of multisource data to estimate downward longwave radiation based on deep neural networks. IEEE Trans. Geosci. Remote Sens. 1-15 https://doi.org/10.1109/TGRS.2021.3094321.
Zhuang, F., Qi, Z., Duan, K., Xi, D., Zhu, Y., Zhu, H., Xiong, H., He, Q., 2021. A comprehensive survey on transfer learning. Proc. IEEE 109, 43–76. https://doi.org/10.1109/JPROC.2020.3004555.